

Advanced computer vision for extracting georeferenced vehicle trajectories from drone imagery

Robert Fonod^{a,*}, Haechan Cho^b, Hwasoo Yeo^b, Nikolas Geroliminis^a

^a*School of Architecture, Civil and Environmental Engineering, École Polytechnique Fédérale de Lausanne (EPFL), Lausanne, CH-1015, Switzerland*

^b*Department of Civil and Environmental Engineering, Korea Advanced Institute of Science and Technology (KAIST), Daejeon, 34141, South Korea*

Abstract

This paper presents a comprehensive framework for extracting georeferenced vehicle trajectories from high-altitude drone footage, addressing key challenges in urban traffic monitoring and limitations of traditional ground-based systems. Our approach employs state-of-the-art computer vision techniques and deep learning models to create an end-to-end pipeline that significantly enhances vehicle detection, tracking, and trajectory stabilization. Conducted in the Songdo International Business District, South Korea, the study utilized a multi-drone experiment over 20 intersections, capturing approximately 12TB of ultra-high-definition video data over four days. We developed a novel track stabilization method that uses detected vehicle bounding boxes as exclusion masks during image registration, which, combined with advanced georeferencing techniques, accurately transforms vehicle coordinates into real-world geographical data. Additionally, our framework includes robust vehicle dimension estimation and detailed road segmentation, allowing for an in-depth analysis of traffic dynamics. The framework produced two high-quality datasets: the Songdo Traffic dataset, comprising nearly 1 million unique vehicle trajectories, and the Songdo Vision dataset, containing over 5,000 human-annotated frames with about 300,000 vehicle instances in four classes. Comparisons between drone-derived data and high-precision sensor data from an instrumented probe vehicle highlight the accuracy and consistency of our framework's extraction in dense urban settings. By publicly releasing these datasets and the pipeline source code, this work sets new benchmarks for data quality, reproducibility, and scalability in traffic research. The results demonstrate the potential of integrating drone technology with advanced computer vision tools for precise and cost-effective urban traffic monitoring, providing valuable resources for the research community to develop intelligent transportation systems and improve traffic management strategies.

Keywords: Drones, Traffic monitoring, Machine vision, Vehicle tracking, Video image processing

1. Introduction

Traditional traffic monitoring methods, such as loop detectors and manual counting, are becoming obsolete in the era of smart cities due to their inflexibility and limited scope [1]. Stationary camera surveillance, although effective, presents economic challenges due to high installation costs and limited field of view (FoV), leading to blind spots. Data from global navigation satellite system (GNSS) and connected vehicles also lack the versatility needed for comprehensive traffic monitoring. Several vehicle detection and tracking technologies have emerged, including camera-based [2–4], LiDAR-based [5, 6], magnetics-based [7, 8], and radar-based [9, 10] systems. While each offers certain advantages, they still face limitations in adaptability and coverage. Accurate estimation of traffic states allows for adjustments in traffic control strategies [11], enhancing network utilization [12, 13], improving road user experiences, and yielding economic and ecological benefits.

The integration of unmanned aerial vehicles (UAVs), commonly known as drones, and computer vision (CV) techniques presents a promising solution to these challenges. Originally developed for military purposes [14], UAVs have

*Corresponding author.

Email addresses: robert.fonod@ieee.org (Robert Fonod), gkqkemwh@kaist.ac.kr (Haechan Cho), hwasoo@kaist.ac.kr (Hwasoo Yeo), nikolas.geroliminis@epfl.ch (Nikolas Geroliminis)

since found applications in various civilian domains, including urban traffic monitoring and management [15–17]. Advances in drone technology, combined with sophisticated CV tools, enable the extraction of detailed vehicle trajectories from high-altitude drone footage, facilitating spatio-temporal analyses of dynamic entities such as vehicles, pedestrians, and cyclists [18–20]. Compared to traditional sensors, these trajectories offer new opportunities for studying complex traffic phenomena, such as large-scale network modeling [21], on-street parking [22], as well as emission [23] and noise [24] estimation. This aerial perspective, free from the constraints of fixed infrastructure, provides an adaptable and cost-effective means to observe urban mobility patterns in congested environments, thereby supporting responsive traffic management strategies in smart cities [25–27].

In a collaborative effort between KAIST and EPFL, a unique multi-drone experiment was conducted in the Songdo International Business District, South Korea, from October 4 to 7, 2022, excluding Monday due to adverse weather conditions. A fleet of 10 commercial-off-the-shelf drones synchronized their operations to monitor 20 busy intersections, as depicted in Fig. 1. Advanced flight plans, combining both hovering and transitioning phases, were executed to optimize coverage. The drones maintained an altitude of 150 meters, with some reduced to 140 meters to mitigate collision risks. Adopting a bird’s-eye view (BEV) perspective, the drones captured footage at 4K ultra-high-definition (UHD) resolution ($3,840 \times 2,160$ pixels) at a smooth frame rate of 29.97 frames per second (FPS). Each day included 10 synchronized flight sessions per drone during peak morning and afternoon periods, each session lasting approximately 30 minutes and followed by a brief battery replacement. This experiment generated 12TB of raw video data and utilized 13 real-time kinematic (RTK)-calibrated ground control points (GCPs) for precise georeferencing. A dedicated drone captured overlapping images at an altitude of 75 meters to create a highly accurate orthophoto of the experiment area, providing a solid foundation for advanced transportation analysis.



Figure 1: Left: Map of the Songdo International Business District, indicating the locations of the 20 monitored intersections labeled A to U (excluding D, which denotes the drones). Right: Images of the 20 intersections as seen by our DJI Mavic 3 drones at 4K resolution.

This work introduces a comprehensive end-to-end trajectory extraction pipeline that employs advanced CV algorithms to derive detailed traffic data from high-altitude drone footage. Although a detailed experiment design and an in-depth analysis of the extracted data are outside this paper’s scope, our contributions significantly expand the resources available to the research community. Specifically, we introduce the *Songdo Traffic* dataset [28], comprising nearly 1 million unique vehicle trajectories, making it one of the largest public traffic datasets collected from a smart city worldwide. This extensive collection provides unparalleled insights into urban mobility, serving as a valuable resource for traffic management and research. The dataset includes trajectory data at a high frequency of 29.97 points per second, complemented by various metadata. Songdo Traffic encompasses vehicle trajectories in multiple coordinate systems (CSs), including global geographic, local Cartesian, and orthophoto CS. Each trajectory is further annotated with metadata such as vehicle identifier (ID), type, and, when feasible, vehicle dimension estimates. Additionally, each trajectory point is tagged with a precise ISO-formatted timestamp, along with instantaneous speed and acceleration estimates, road section and lane number information, and a visibility flag, where available.

Complementing Songdo Traffic, the *Songdo Vision* dataset [29] addresses the scarcity of detailed vehicle annotations necessary for training object detection models, particularly from high-altitude BEV aerial perspectives, where smaller vehicles, like motorcycles, are often less discernible. This dataset contains over 5,000 human-annotated video frames, featuring nearly 300,000 vehicle instances across four distinct classes: cars (including vans and light-duty vehicles), buses, trucks, and motorcycles. To facilitate broader use, annotations are provided in multiple formats compatible with

various deep learning (DL) models, making the Songdo Vision dataset a valuable resource for improving and validating vehicle detection algorithms. Our commitment to open science drives us to release these datasets [28, 29] alongside the source codes [30–32] for our extraction and stabilization routines. These resources are poised to set new benchmarks for data quality and reproducibility in traffic research that leverages CV and DL techniques.

Our extraction methodology introduces several innovative techniques that significantly enhance the accuracy and reliability of vehicle trajectory data from drone imagery. Firstly, we trained a highly accurate object detector using a state-of-the-art (SOTA) model architecture with the Songdo Vision dataset, supplemented by eight curated public datasets, resulting in superior detection performance as validated on the Songdo Vision test set. Secondly, to address the challenges of drone movements, we developed a novel track stabilization method that uses detected vehicle bounding boxes (BBs) as no-feature masks during image registration, thereby improving stabilization accuracy and computational efficiency. Additionally, we introduce a robust vehicle dimension estimation that uses azimuth-based filtering and ratio-based criteria to ensure accurate measurements under varying conditions. Our methodology further includes comprehensive speed and acceleration computation, incorporating visibility filtering and Gaussian smoothing to derive realistic traffic dynamics. Advanced georeferencing techniques, employing a high-resolution orthophoto enhanced with 13 ground control points, ensure precise mapping of trajectories into real-world coordinates. We optimized the orthophoto creation and image registration through an extensive parameter search, resulting in highly accurate geospatial data for traffic analysis.

During the Songdo experiment, various traffic events, including severe congestion and post-accident traffic dynamics, were captured alongside an instrumented autonomous vehicle (AV) from Stanford University equipped with high-precision real-time kinematic GNSS (RTK-GNSS) sensors. Although the collision itself occurred during a battery swap and was not recorded, the prolonged presence of the involved vehicles allowed us to capture the resulting traffic disruptions over time. The AV data provided a valuable resource for comparison with our drone-derived trajectories and speed profiles, demonstrating very high consistency between the two measurement methods. Furthermore, our methodology underwent rigorous hyperparameter tuning for track stabilization and a series of benchmarks to assess image registration and georeferencing accuracy. For vehicle dimension estimation, our results closely aligned with known dimensions of specific vehicles, such as the AV and recognizable bus types, confirming the method’s capability to produce realistic distributions.

By addressing key challenges in drone-based traffic monitoring through CV, as discussed in [Section 2](#), this research presents a comprehensive end-to-end framework for extracting georeferenced trajectories from high-altitude drone footage. We enhance detection and tracking algorithms to handle unique perspectives and dynamic conditions, surpassing traditional ground-based methods. Our innovative track stabilization, accurate vehicle dimension estimation, speed and acceleration computations, and precise georeferencing contribute to the extraction of high-quality trajectory data. Comparison with AV data shows that our methods produce realistic speed, acceleration, and dimension distributions. By disseminating these methods through open-source datasets and code, we establish a new resource for data quality, facilitating more responsive, scalable, and cost-effective traffic management solutions in smart cities.

2. Related work

This section reviews the SOTA in drone-based traffic data extraction, including object detection, tracking, video stabilization, georeferencing, and dataset availability. Traditional CV methods for fixed cameras, such as background subtraction [33], optical flow (OF) [34], template matching [35], feature matching [36], and histogram-based methods [37, 38], face challenges in complex environments [39] and under varying illumination conditions [4, 40, 41].

2.1. Object detection

The rise of DL techniques for CV has significantly improved vehicle detection. Leading architectures include single shot detector (SSD) [42], region-based convolutional neural network (R-CNN) [43], and you only look once (YOLO) [44]. R-CNN variants, such as Faster R-CNN [45], have been used for vehicle detection in various studies [46, 47]. YOLO models (v3–v10) [48–55] have also been adapted for accuracy in traffic surveillance [17, 56, 57].

Despite their effectiveness, these models often rely on non-maximum suppression (NMS), introducing post-processing complexities. Recent transformer-based detectors (DETRs) [58–61] aim to eliminate NMS but struggle with small object detection and require high computational resources. Specialized detectors, such as YOLO for occluded vehicles [62] and the Butterfly detector [63], address challenges specific to aerial perspectives. Integration of multi-modal data, like combining RGB with LiDAR [64] or thermal [65] imaging, has also shown promise in enhancing detection in complex urban environments.

2.2. Object tracking

Accurate tracking is essential for reliable movement data. Traditional methods [66], like Kalman filtering [67] and the Hungarian algorithm [68], have been widely used in traffic analysis [47, 69–71]. However, these approaches often struggle with drone-captured footage complexities, especially in dynamic urban environments where occlusions, varying object sizes, and diverse motion patterns pose significant challenges.

Modern multi-object tracking (MOT) algorithms, such as simple online and realtime tracking (SORT) [72], observation-centric SORT (OC-SORT) [73], ByteTrack [74], and “bag of tricks” SORT (BoT-SORT) [75], follow the separate detection and tracking (SDP) paradigm. Hybrid models, including DeepSORT [76], StrongSORT [77], and BoT-SORT-ReID [75], incorporate appearance information to reduce identity switches and handle occlusions more effectively. End-to-end tracking approaches like FairMOT [78] combine detection and tracking but face challenges in BEV perspectives due to limited ground truth data and high computational demands.

Current challenges in MOT include persistent track loss in occluded areas, object similarity, and high computational costs. These issues may be particularly acute in dense urban environments. While benchmarks like MOTChallenge [79–81] have advanced pedestrian tracking, vehicle tracking in BEV contexts remains underrepresented.

2.3. Stabilization

Unlike larger drones equipped with high-performance gimbals, video stabilization is crucial for accurate traffic data extraction with smaller commercial drones that are more susceptible to environmental disturbances like wind [82, 83]. Stabilization, a form of video registration [84], involves aligning consecutive frames by matching keypoints to correct unwanted motion. Various keypoint detectors such as scale-invariant feature transform (SIFT) [85], root SIFT (RSIFT) [86], binary robust invariant scalable keypoints (BRISK) [87], KAZE [88], accelerated-KAZE (A-KAZE) [89], and oriented FAST and rotated BRIEF (ORB) [90] are commonly used. OF methods, like the Kanade-Lucas-Tomasi (KLT) tracker [91], are faster but can be less reliable [92]. Recent DL-based methods such as SuperPoint [93] and SuperGlue [94] enhance keypoint detection and matching, although they often require fine-tuning with ground truth data.

Keyframe correspondences established through these features allow for the computation of either perspective or affine transformations using the least squares method, optimized by variants of the random sample consensus (RANSAC) algorithm [95] for outlier rejection. Feature matching algorithms, such as brute force (BF) or fast library for approximate nearest neighbors (FLANN) [96], compute similarity scores between extracted keypoints to form correspondences. Pre-processing steps, like grayscale conversion and contrast limited adaptive histogram equalization (CLAHE), are implemented to enhance keypoint detection in varying lighting conditions.

Various methods can be combined to align video frames, allowing for smoother vehicle tracking. For instance, [82] utilized speeded-up robust features (SURF) features for keypoint detection to ensure smooth traffic analysis. However, the main challenge in stabilization is achieving an optimal balance between speed and accuracy while mitigating distortions caused by moving objects.

2.4. Georeferencing

Georeferencing is crucial for converting trajectories into real-world coordinates. Accurate georegistration often requires a precise georeferenced image of the area [84, 97, 98]. An orthophoto, a geometrically corrected (orthorectified) image that eliminates distortions caused by camera tilt, lens distortion, and topographic relief, is a prevalent method for this purpose [99]. This correction allows orthophotos to represent true distances accurately, making them essential for measurements and analyses. Nonetheless, previous studies often omit meticulous consideration of accurate georeferencing, relying on simplistic methods based on ground sample distance (GSD) for estimating only a subset of traffic parameters, such as vehicle speed and location derived from drone’s location and GSD-scaled image coordinates. However, these methods lack the accuracy required for traffic monitoring, particularly since commercial-off-the-shelf drones often exhibit positional errors greater than claimed [100].

More sophisticated georeferencing involves the use of geographic information system (GIS) software [17] for manual alignment of imagery. While more accurate than basic GSD methods, this approach is time-consuming and demands significant expertise. Alternatively, the use of RTK-GNSS significantly enhances georeferencing accuracy by refining both the GCPs placement and the drone’s position during image capture. RTK-GNSS achieves centimeter-level precision through corrections provided by a nearby base station, thereby facilitating the generation of highly accurate orthophotos for the surveyed area.

By combining accurate orthophotos with automatic image matchings, georeferencing becomes more precise, reducing the reliance on manual interventions. This process not only streamlines the trajectory extraction pipeline but also addresses the inaccuracies commonly associated with GSD or GIS-based methods, enabling more reliable mapping of vehicle movements in real-world coordinates.

2.5. Availability of datasets

Recent datasets like HighD [101], HARPY [102], pNEUMA [27], and CitySim [103] focus on specific traffic scenarios, such as single intersections or highway segments, and often use outdated CV methods. HighD and HARPY, for instance, utilized U-Net and YOLOv2 for detection but lacked robust trajectory validation. pNEUMA, which employed static drone swarms, provides insights into traffic flow but experiences imprecise BBs and trajectory anomalies [20, 104], possibly due to visual limitations or suboptimal CV tools. Meanwhile, CitySim’s methodologies, including its georeferencing algorithm, remain undisclosed, and its traffic data lacks validation.

Vehicle annotation datasets, such as CARPK [105], CyCAR [106], HARPY [107], RAI4VD [108], UAVDT [109], UIT-ADrone [110], and VisDrone [111], serve as valuable resources for object detection training. However, they often employ basic annotation techniques and cover a limited, sometimes inconsistent, range of vehicle classes. This variability in annotation accuracy can impact the data’s reliability for training DL models.

2.6. Summary

In summary, while the potential of drones and CV in urban traffic data extraction is evident, challenges such as diverse object scales, occlusions, and the scarcity of comprehensive datasets persist [4, 112]. Most existing approaches are optimized for static cameras and lower altitudes, limiting their effectiveness in BEV perspectives, where objects appear smaller and less distinctive. Video stabilization and georeferencing are critical for enhancing extraction pipelines. However, common methods like GSD-based and manual GIS georeferencing often fall short in accuracy. Incorporating RTK-GNSS for orthorectification with GCPs and advanced stabilization techniques enables more reliable trajectory extraction from high-altitude drone imagery. These advancements, coupled with improved datasets, can significantly contribute to effective traffic monitoring and urban planning.

3. Methodology

Our methodology for transforming raw drone footage into detailed traffic data, which is compiled into the Songdo Traffic dataset, involves several key steps, as shown in [Fig. 2](#). First, in the data wrangling step, the raw videos are processed into meaningful segments. In parallel, selected frames are annotated to identify vehicle classes, which are used to train and validate an object detection algorithm, and are released as part of the Songdo Vision dataset. The detection algorithm processes the segmented videos to detect and locate vehicles. Next, a MOT algorithm assigns unique IDs and tracks vehicles across frames. Image registration methods stabilize the footage and transform vehicle coordinates into a fixed reference frame. Georeferencing then converts these coordinates into real-world values using homographic and affine transformations, along with an orthophoto. Finally, the extracted trajectories are used to derive useful metadata, including vehicle dimensions, speed, acceleration, road segment, and lane number. By applying track stabilization after object tracking, we are able to bypass the limitations of traditional video stabilization and achieve more accurate results.

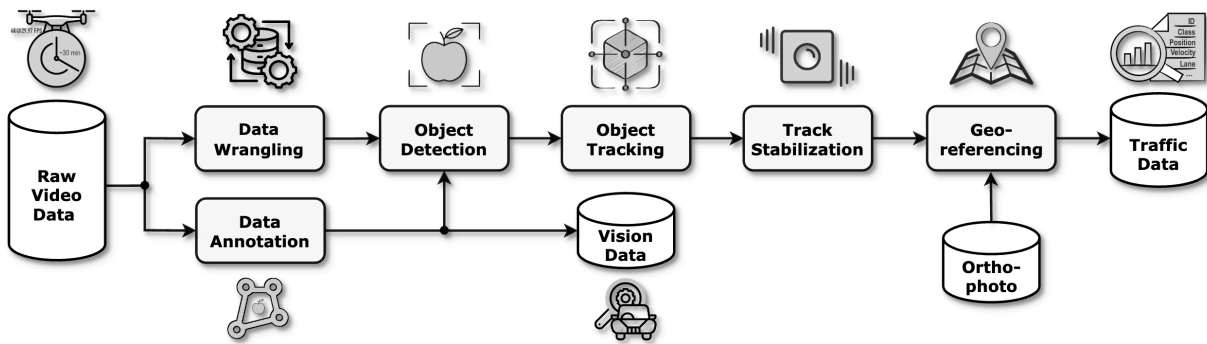


Figure 2: Diagram illustrating the vehicle trajectory extraction process from raw drone footage to traffic data, with auxiliary human annotation and vision data generation.

3.1. Data wrangling

During the data wrangling phase, we segmented 12TB of raw UHD drone videos, saved in .mp4 format at 29.97 FPS, along with their corresponding flight logs, into distinct segments. Each video segment corresponds to a stable hovering period of an individual drone over a monitored intersection (see [Fig. 1](#)).

The raw videos, fragmented due to the drone’s limitation to keep individual files under 4GB, along with the corresponding flight logs, were first merged into 30-minute segments for each flight session. These merged files contained both stationary footage at intersections and dynamic clips of drones transitioning between intersections or during take-offs and landings. Since yaw measurements were missing in the flight logs, manual segmentation by human annotators was required to remove transient or rotational movements caused by technical glitches or human error, ensuring that only stable footage was retained. Hovering periods with significant drone movements were also split during this process.

After manual segmentation, an automated process cut the footage at the nearest I-frame (intra-coded frame, a type of video frame that contains a complete image and serves as a key reference point for efficient video compression) to avoid re-encoding, significantly speeding up the editing process. The segmented files were then organized using an automated naming system. Each file name includes an intersection label (see [Fig. 1](#)), automatically determined by matching the average latitude and longitude from the flight logs with the nearest intersection center. A unique sequence number is also appended to identify each hovering event, resetting at the start of each flight session. Due to the optimized flight paths, video lengths varied, typically ranging from 2 to 4 minutes, depending on the drone and intersection.

3.2. Data annotation

The unique challenges of the Songdo study, particularly the BEV aerial perspective at 140-150m altitudes, required the creation of a specialized vehicle annotation dataset. Existing public datasets often lack the necessary quality, with varying perspectives, resolutions, and object sizes that do not align with our study’s specific conditions. Additionally, their annotations are frequently inaccurate, with poor-quality BBs that can compromise the performance of detection models. To ensure reliable object detection directly within the Songdo experiment’s environment, we constructed a custom dataset tailored to our specific needs.

Our dataset categorizes vehicles into four classes: cars (including vans and light-duty vehicles), buses, trucks, and motorcycles, specifically designed to enhance model training and evaluation (see [Section 3.3](#)). By integrating diverse scenes from multiple public datasets, we aimed to improve the model’s accuracy and robustness for our task. A total of 5,419 video frames were annotated, capturing nearly 300,000 vehicle instances with tight, axis-aligned BBs, see examples in [Fig. 3](#) (left). The annotations, summarized in [Table 2](#), were conducted by trained annotators using Azure ML Studio to maximize precision. Following open science principles, the Songdo Vision dataset will be made publicly available alongside the traffic dataset.



Figure 3: Left: Examples of human-annotated frames. Right: Examples of underrepresented motorcycle instances.

Of the total frames annotated, 5,274 were randomly selected from the merged drone videos (described in [Section 3.1](#)), covering both hovering and transitioning sequences. The remaining 145 frames were carefully chosen to include underrepresented scenarios, such as motorcycles at pedestrian crossings, bicycle lanes, near traffic light poles, and other distinctive road markers, as shown in [Fig. 3](#) (right). This selection process was meticulously managed to include only footage from suitable altitudes and camera angles, ensuring the integrity and accuracy of the dataset.

The Songdo Vision dataset, enriched with human-verified annotations, aims to significantly improve vehicle detection algorithms, providing a reliable ground truth for model validation. We plan to release the annotations in widely-used formats such as COCO, YOLO, and Pascal VOC, ensuring compatibility with a broad range of applications beyond traffic analysis, including autonomous drone delivery, surveillance, safety systems, and environmental studies.

3.3. Object detection

Object detection is a pivotal component of our vehicle extraction framework. We employ a DL-based object detector that predicts BBs encoded as (x, y, w, h) . Here, (x, y) represent the center coordinates of the BB, while w and h denote its width and height, respectively. Each k -th image frame of video v , denoted F_v^k , is a $w_I \times h_I$ matrix of pixel intensities, where w_I and h_I represent the frame's width and height in pixels, respectively.

Our object detector processes each frame F_v^k to identify potential vehicles by predicting BBs. Following this initial detection step, our pipeline employs a class-agnostic NMS algorithm with an intersection over union (IoU) threshold $\eta_{\text{IoU}} > 0$. This crucial step effectively eliminates overlaps among the BBs, thereby refining the overall detection quality in densely populated urban settings. The refined set of detections, $\mathcal{D}_v[k]$, includes only the most reliable vehicle detections and is defined as follows:

$$\mathcal{D}_v[k] = \left\{ \left(x^{(i)}[k], y^{(i)}[k], w^{(i)}[k], h^{(i)}[k], c^{(i)}[k], s^{(i)}[k] \right) \mid s^{(i)}[k] \geq \tau_d \right\}_{i=1}^{N_v^d[k]}, \quad (1)$$

where $N_v^d[k]$ represents the number of vehicle detections in the k -th frame after processing through NMS. For the i -th detection, $x^{(i)}$ and $y^{(i)}$ are the normalized center coordinates of the BB, $w^{(i)}$ and $h^{(i)}$ are its normalized width and height, $c^{(i)}$ is the class label restricted to $c^{(i)} \in C = \{0, 1, 2, \dots, C-1\}$, with $C > 0$ representing the total number of distinct object classes recognized by the detector, and $s^{(i)}$ is the confidence score constrained within $(0, 1]$. Detections are retained in $\mathcal{D}_v[k]$ only if their confidence scores exceed the detection threshold $\tau_d > 0$. All BB coordinates and dimensions are normalized with respect to the input image size, ensuring that $0 \leq x^{(i)}, y^{(i)}, w^{(i)}, h^{(i)} \leq 1$.

We employed the anchor-free YOLOv8 detector architecture [53], which has demonstrated superior performance across all metrics, establishing it as one of the top-performing object detectors available at the onset of our research. Compared to the anchor-based YOLOv5 [50] and transformer-based real-time DETR (RT-DETR) [61], YOLOv8 offers enhanced accuracy and faster inference speeds, particularly for smaller object, making it more suitable for our operational requirements. After extensive trials, the ‘s’ model scale with standard output heads was selected for its optimal balance of accuracy and inference speed. While we experimented with an additional P2/4 output layer, as utilized in our previous YOLOv5 setup[17], no significant performance gains were observed within the YOLOv8 architecture. This architecture was ultimately configured with $\tau_d = 0.25$ and $\eta_{\text{IoU}} = 0.7$.

Our object detector was trained using a multi-stage approach. Initially, the model was trained on the large-scale “BASE” dataset, which consists of a diverse collection of images from various sources, offering broad coverage of vehicle types and scenarios. This training commenced with weights pre-trained on the COCO dataset [113], establishing a solid foundation for transfer learning. Subsequently, the model was fine-tuned on the “FINE” dataset, a curated, high-quality subset of BASE, specifically chosen for its accurate annotations and higher-resolution images, facilitating fine-grained model refinement. The datasets, which include images and vehicle annotations from eight public datasets and our own Songdo Vision dataset (described in Section 3.2), are further detailed in Table 1. The BASE and FINE datasets comprised 21,908 and 10,187 images, respectively, with 3,458 images from BASE and 1,183 images from FINE designated for testing, while the remaining images were utilized for training.

Table 1: Datasets employed in multi-stage training.

Dataset	BASE	FINE	Consolidated class labels	Present but not annotated
Songdo Vision [29]	✓	✓	Car, bus, truck, motorcycle	Pedestrian, bicycle
CARPK [105]	✓	✗	Car	Motorcycle, pedestrian
PUCPR+ [105]	✓	✗	Car	Motorcycle, pedestrian
CyCAR [106]	✓	✓	Car	
UAVDT [109]	✓	✗	Car, bus, truck	Motorcycle, pedestrian
HARPY [107]	✓	✗	Car, bus, truck	
RAI4VD [108]	✓	✓	Car, bus, truck, motorcycle	Pedestrian
UIT-ADrone [110]	✓	✓	Car, bus, truck, motorcycle, pedestrian, bicycle	
VisDrone [111]	✓	✗	Car, bus, truck, motorcycle, pedestrian, bicycle	

To ensure that our FINE dataset met stringent training specifications, we excluded certain datasets, such as VisDrone and UAVDT. For example, VisDrone’s annotations primarily originate from non-BEV environments at lower altitudes, resulting in inconsistent object size representations and varied camera settings that complicated integration. Additionally, this dataset exhibited mediocre annotation accuracy, further justifying its exclusion from our FINE dataset.

The eight public datasets we sourced include a variety of aerial images, characterized by varying altitudes, camera angles, perspectives, resolutions, illumination conditions, image quality, and train/test split ratios. To ensure consistency

with our 140m – 150m BEV scenes in Songdo, we performed extensive preprocessing and filtering of these datasets. Although a comprehensive description of these steps is omitted here for brevity, we focused on consolidating the diverse class labels found in the public datasets to streamline our trajectory extraction process, which utilizes four primary vehicle categories and two auxiliary categories: $C = \{0, 1, 2, 3, 4, 5\}$, where 0 corresponds to cars (including vans and light-duty vehicles), 1 to buses, 2 to trucks, 3 to motorcycles, 4 to pedestrians, and 5 to bicycles. While only the four primary vehicle categories were used during inference, the auxiliary categories (pedestrians and bicycles) were retained during training to improve overall classification performance.

Although pedestrians and bicycles were excluded during inference due to their underrepresentation in the training data (see [Table 2](#)) and diminutive sizes, we included them in the training phase with the aim of reducing false positives from similarly sized objects like motorcycles and improving the model’s ability to distinguish between closely related categories. To ensure consistency and enhance reliability, certain object classes in the public datasets were either disregarded or consolidated into the categories defined by C . For instance, in the VisDrone dataset [111], where “pedestrian” and “people” are distinct labels, these categories were merged into a single “pedestrian” label, while classes like tricycles (including awning-tricycles) were excluded. Additionally, since vans were treated as a separate class in some datasets but included under cars in others, we uniformly combined vans with cars across all datasets to standardize detection.

Table 2: Annotation counts and class distribution across training and test sets for the considered datasets.

Vehicle class	BASE dataset			FINE dataset			Songdo Vision dataset		
	Training	Test	Test ratio	Training	Test	Test ratio	Training	Test	Test ratio
All	679,306	169,183	19.9 %	321,368	68,102	17.5 %	217,311	55,124	20.2 %
Car	561,666	148,375	20.9 %	266,745	52,260	16.4 %	195,539	49,508	20.2 %
Bus	15,587	2,202	12.4 %	8,047	1,793	18.2 %	7,030	1,759	20.0 %
Truck	28,830	4,869	14.4 %	14,305	3,452	19.4 %	11,779	3,052	20.6 %
Motorcycle	44,512	11,478	20.5 %	30,925	10,309	25.0 %	2,963	805	21.4 %
Pedestrian	24,239	1,983	7.6 %	1,260	243	16.2 %		N/A	
Bicycle	4,472	276	5.8 %	86	45	34.4 %		N/A	

To optimize our object detection for the complex and variable conditions of drone-based surveillance, we employed a comprehensive suite of data augmentation strategies. These included random scaling, translations, rotations, and left-right flips, along with random adjustments to hue, saturation, and brightness with factors of 0.015, 0.7, and 0.4, respectively. Additionally, we applied mosaic augmentation with a probability of 1.0, which combines four different training images into a single composite image. This approach has been shown to enhance the model’s ability to generalize across different scenes and object scales by introducing diverse spatial relationships and object sizes within a single training instance [114]. All these strategies were essential for adapting the model to real-world variations in vehicle appearance caused by changing lighting conditions, weather, and diverse urban landscapes.

Our training strategy employed stochastic gradient descent (SGD) optimization with YOLOv8’s default hyperparameters, including an initial learning rate of 0.01, a final learning rate factor of 0.01, a momentum of 0.937, and a weight decay of 0.0005 to mitigate overfitting. Although several hyperparameter configurations were explored, the default settings ultimately yielded the best performance. A batch size of 8 was utilized, with early stopping implemented at a patience of 50 epochs. Automatic mixed precision was enabled to enhance computational efficiency without compromising model accuracy. The loss function was calibrated with box, classification, and direction field loss gains of 7.5, 0.5, and 1.5, respectively. Consistent input resolution of $1,920 \times 1,920$ pixels was maintained during both training and inference, employing letterbox padding to preserve aspect ratio and ensure uniform feature representation across different scenes. This relatively high resolution was essential for capturing fine details and achieving acceptable performance in detecting small objects like motorcycles.

Songdo Vision, comprising 5,419 annotated images, was split into training and test sets, with 20% (1,084 images) designated as the test set, allocated for both model validation during training and final testing of our top-performing object detector. [Table 2](#) shows the class distribution across the sets. Our top-performing model was selected based on its highest mean Average Precision (mAP) at an IoU of 0.5 (mAP@50) across all classes. As shown in [Table 3](#), this model demonstrated remarkable performance across all vehicle types, achieving an exceptional mAP@50 of 0.888 for motorcycles, despite their smaller pixel size. These results highlight the model’s robustness in detecting small objects in BEV drone videos. To briefly define the key metrics: Precision indicates the proportion of correctly identified vehicles out of the total detected, while Recall reflects the ratio of correct detections to the actual number of vehicles in a class. The mAP@50 measures detection accuracy using an IoU threshold of 0.5, and mAP@50-95 evaluates performance over a range of IoU thresholds (0.5 to 0.95), with a step size of 0.05, capturing variability in BB overlaps.

Table 3: Detection performance metrics assessed using Songdo test set.

Class	Precision	Recall	mAP@50	mAP@50-95
All	0.911	0.935	0.951	0.711
Car	0.979	0.981	0.992	0.835
Bus	0.952	0.977	0.988	0.826
Truck	0.887	0.916	0.935	0.722
Motorcycle	0.827	0.866	0.888	0.463

The confusion matrix in Fig. 4 (left) reveals the model’s classification performance, highlighting accurate predictions and class-specific misclassification. The precision-recall curve in Fig. 4 (right) demonstrates a low rate of false positives and negatives, indicating strong object detection performance. While the model occasionally misclassifies smaller objects like pedestrians or bicycles as motorcycles, especially near pedestrian crossings or bike lanes, we have not attempted to filter out these rare cases due to the complexity involved in accurate differentiation. Despite this, the model’s performance on motorcycles, though slightly lower than for larger vehicles, highlights the challenges of detecting smaller objects in drone footage.

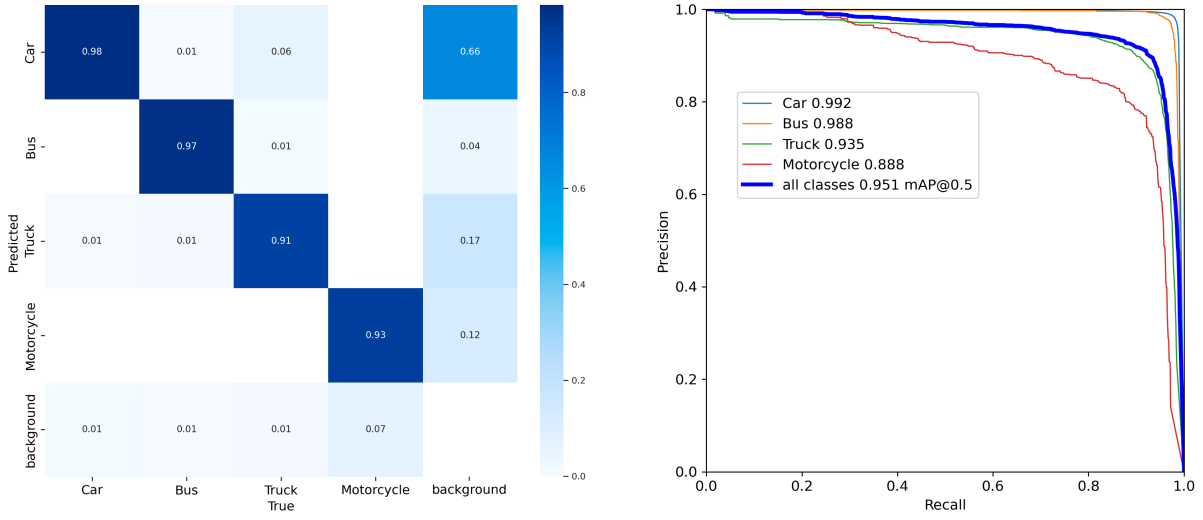


Figure 4: Left: Normalized confusion matrix. Right: Precision-recall curve.

In conclusion, our object detection system has demonstrated robust performance in identifying various vehicle types in drone-based surveillance. While our current model faces challenges in detecting smaller objects like pedestrians and cyclists, we are actively exploring strategies to address these limitations. By incorporating data augmentation techniques, investigating advanced algorithms, and leveraging newly emerging datasets with more comprehensive annotations, we aim to enhance the system’s capabilities.

3.4. Object tracking

Object tracking, specifically MOT, is a crucial component of our framework, assigning unique IDs to each vehicle and consistently tracking their movements across video frames. This enables continuous tracking, even during temporary occlusions, providing valuable insights into vehicle behavior and interactions over time.

For the k -th frame of video v , the MOT algorithm processes the detection set $\mathcal{D}_v[k]$ to generate a set $\mathcal{T}_v[k]$ of $N_v^t[k]$ tracks, each represented as:

$$\mathcal{T}_v[k] = \left\{ (id^{(i)}[k], x^{(i)}[k], y^{(i)}[k], w^{(i)}[k], h^{(i)}[k], c^{(i)}[k], s^{(i)}[k]) \in \mathcal{I}_v[k] \times \mathcal{D}_v[k] \right\}_{i=1}^{N_v^t[k]}, \quad (2)$$

where ' \times ' denotes the Cartesian product, $\mathcal{I}_v[k]$ is the set of unique vehicle IDs in v up to frame k , and $id^{(i)}[k] \in \{1, 2, \dots, V_v[k]\}$ is the unique ID for each tracked vehicle, consistent across all frames. The number of active tracks in $\mathcal{T}_v[k]$ is $N_v^t[k]$, while $V_v[k]$ is the total number of unique vehicles observed up to frame k . The remaining symbols in Eq. 2 have the same meanings as in Eq. 1.

After applying tracking to all frames F_v^k , $k \in \{1, \dots, N_v\}$, where N_v is the total number of frames in v , we implement a class label refinement step for $c^{(i)}[k]$ in $\mathcal{T}_v[k]$ to maintain classification consistency across frames for each tracked vehicle. Although our observations indicate such inconsistencies are very rare, we formalize this refinement through the following aggregation function:

$$f_c(\text{id}) = \arg \max_{c \in C} \left\{ \sum_{k=1}^{N_v} \sum_{i=1}^{N_v^i[k]} s^{(i)}[k] \cdot \mathbf{1}(c^{(i)}[k] = c) \cdot \mathbf{1}(id^{(i)}[k] = \text{id}) \right\}, \quad \text{id} = 1, \dots, V_v[N_v], \quad (3)$$

where $\mathbf{1}(\cdot)$ is the indicator function that is 1 if the condition is true and 0 otherwise. In this process, for each vehicle ID, the ultimate class label is assigned by selecting the class $c \in C$ that maximizes the sum of confidence scores across all frames where that ID appears, that is, we refine the class labels to $c^{(i)}[k] = f_c(id^{(i)}[k])$.

The MOT algorithm efficiently manages the assignment of new IDs and the removal of vehicles that no longer appear in the frame. Consequently, $N_v^i[k] \leq V_v[k]$ is maintained for all frames. In case of intermittent tracking failures, such as those due to prolonged visual occlusions or prolonged misdetections, the resulting vehicle trajectory may exhibit multiple assigned IDs. However, this occurrence has minimal impact on the primary goal of our effort, which is the extraction of precise trajectories. Furthermore, such instances are relatively infrequent, predominantly attributed to motorcycles that traverse complex road infrastructure, as illustrated in [Fig. 3](#) (right).

To effectively address the challenges posed by intermittent tracking failures and to ensure the continuity and accuracy of vehicle tracking, we adopted the BoT-SORT algorithm [75] within our tracking framework. As part of the SDP class, BoT-SORT, an enhancement over the original ByteTrack [74], incorporates a suite of optimizations, notably including an improved Kalman filter state vector and efficient ego motion compensation (EMC). These enhancements elevate BoT-SORT to a SOTA status, especially noted for its adaptability in dynamic environments and its exceptional capability to reduce identity switches and tracking failures [75]. Crucially, BoT-SORT has shown remarkable efficacy in managing sporadic misdetections, a frequent issue with fast-moving and smaller vehicles such as motorcycles, which are often underrepresented in aerial datasets. This made it the ideal choice for our tracking needs, particularly in scenarios with minimal occlusions, where the comprehensive integration of a Re-ID module would not deliver proportional benefits.

To regulate the frequency of misdetections leading to ID deletion, we employ a track buffer of $T_{\text{buff}} = 30$ frames, which retains information about tracks that may temporarily disappear, for example, due to occlusion or miss-detection. This buffer is essential for managing tracks in environments prone to visual interruptions, ensuring that vehicles that may reappear are not prematurely removed from tracking. However, in our Songdo experiment, the importance of this buffer is minimal since obstructions are limited to a few small bridges. These are situated away from the main road arteries and intersections, as shown in [Fig. 1](#), typically occurring at exit roads from underground garages that lead onto the main road.

Additionally, the BoT-SORT algorithm employs several thresholds to manage track initiation and termination. A new track is initiated when a detection's confidence score exceeds τ_n , ensuring only high-confidence detections contribute to track formation. For our implementation, we set $\tau_n = 0.6$. For track termination, a dual-threshold strategy is implemented: high-confidence matches are made above $\tau_h = 0.5$, while low-confidence matches are allowed above $\tau_l = 0.1$. Furthermore, associations between detections and existing tracks are ensured by a matching threshold of $\tau_m = 0.8$, providing robust track management. Additionally, BoT-SORT employs an efficient EMC method based on sparse OF to adjust the tracking during camera movements, compensating for the global background motion that might otherwise introduce errors. This capability allows us to apply track stabilization as a subsequent step after object tracking, rather than relying on traditional video stabilization earlier in the pipeline, as shown in [Fig. 2](#). The advantages of this approach to trajectory stabilization are further discussed in [Section 3.5](#).

Although BoT-SORT was originally validated on pedestrian tracking in street-level perspectives through the MOT Challenge dataset [75], multiple factors support its reliability in our aerial vehicle tracking application. First, our setup benefits from favorable tracking conditions: the combination of 4K resolution footage captured at high-frequency 29.97 FPS and vehicles moving at speeds normally not exceeding 80 km/h ensures sufficient frame-to-frame overlap for robust tracking. Second, qualitative validation through manual inspection of randomly sampled trajectories showed perfect tracking consistency across all examined cases. Finally, our AV experiment (detailed in [Section 4.2](#)) provides quantitative validation of the tracking precision, as we successfully matched multiple ground truth trajectories of the AVs with their corresponding tracked sequences.

3.5. Track stabilization

To mitigate the effect of drone movements on the extracted trajectories, we “stabilize” each track $\mathcal{T}_v[k]$ by aligning the coordinates of each frame F_v^k ($k = 2, \dots, N_v$) with a reference frame F_v^{ref} , which is set as the first frame of the video v , i.e., $F_v^{\text{ref}} \triangleq F_v^1$. This ensures consistent alignment throughout the footage. As illustrated in [Fig. 5](#), we achieve this alignment

through image registration by identifying corresponding keypoints between pairs of grayscale frames (F_v^{ref} and F_v^k), with optional CLAHE applied to improve contrast. The matched keypoints are used to compute a 3×3 homography matrix $H_v^{k \rightarrow \text{ref}}$ using the least squares method, enhanced with a variant of the RANSAC algorithm to reject outliers. Despite the marginally higher computational cost, we choose a projective transformation over an affine one to more effectively account for potential camera tilting caused by wind.

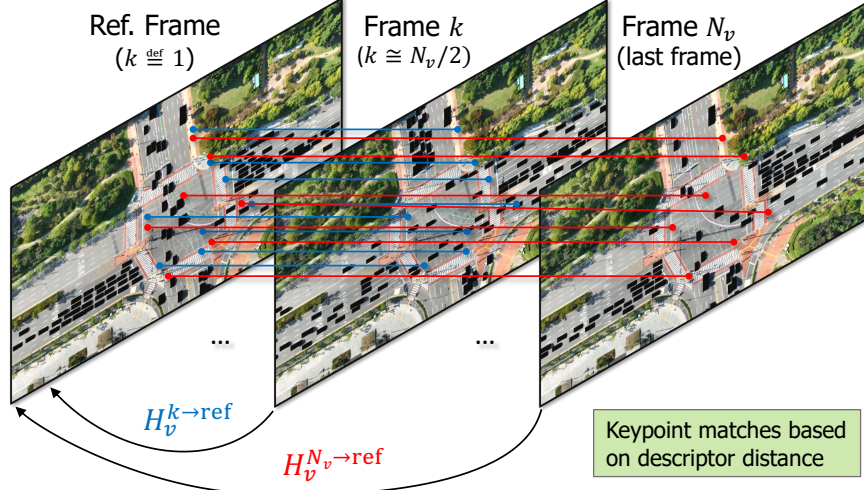


Figure 5: Illustration of the image registration process. Keypoints from static background features are matched between frames and used to compute a homography matrix $H_v^{k \rightarrow \text{ref}}$ to align the frames. Exclusion masks prevent keypoint detection in dynamic vehicle regions, ensuring stable matching.

3.5.1. Implementation details

We extract up to K and K_{ref} keypoints from each frame F_v^k ($k = 2, \dots, N_v$) and the reference frame F_v^{ref} , respectively, using a local feature detector. To ensure stable frame alignment, we focus keypoint detection on static background elements by leveraging the BBs from $\mathcal{D}_v[k]$ as “exclusion masks”. These masks prevent keypoint detection within vehicle regions, which would otherwise introduce unstable matches due to vehicle movement. To account for potential inaccuracies in BBs, each box is enlarged by a factor $\epsilon > 0$, adjusting mask dimensions to $\tilde{w} = w(1 + \epsilon)$ and $\tilde{h} = h(1 + \epsilon)$.

Keypoint matches between each pair $(F_v^{\text{ref}}, F_v^k)$ are identified based on a similarity measure calculated from keypoint descriptors, typically using Euclidean distance or cosine similarity, depending on the descriptor type. These potential matches, denoted as $m_v^{k \rightarrow \text{ref}}$, are refined using Lowe’s ratio test [85], also known as second nearest neighbors (SNN) test, which filters out non-discriminative matches using a threshold $\theta_{\text{SNN}} \in (0, 1]$, resulting in a refined match set $\tilde{m}_v^{k \rightarrow \text{ref}}$. This refined set is then used by a robust estimator to compute the homography matrix $H_v^{k \rightarrow \text{ref}}$. The confidence level τ , the maximum number of iterations Γ , and the epipolar threshold η are tuning parameters for most RANSAC algorithms. To reduce computational load when determining homography matrices, we downscale the 4K input frames F_v^k ($k = 1, \dots, N_v$) using a scale factor ρ , resulting in adjusted frame dimensions $\tilde{w}_I = \rho \times w_I$ and $\tilde{h}_I = \rho \times h_I$.

The derived homography matrix $H_v^{k \rightarrow \text{ref}}$ can transform any pixel coordinates from frame F_v^k to the reference frame. For a generic point $p_v^k = [x, y]^T$ in frame F_v^k , its corresponding location in the reference frame is:

$$p_v^{\text{ref}} = \begin{bmatrix} x_{\text{ref}} & y_{\text{ref}} \end{bmatrix}^T = \begin{bmatrix} x'/z & y'/z \end{bmatrix}^T, \quad (4)$$

where

$$\begin{bmatrix} x' & y' & z \end{bmatrix}^T = H_v^{k \rightarrow \text{ref}} \begin{bmatrix} x & y & 1 \end{bmatrix}^T. \quad (5)$$

Here, the point p_v^k is converted to homogeneous coordinates by appending 1, the homography is applied, and the result is normalized by dividing by z . This transformation can be concisely represented as $p_v^{\text{ref}} = H_v^{k \rightarrow \text{ref}}(p_v^k)$, directly mapping each point from the original frame to its position in the reference frame.

In our track stabilization approach, we apply these transformations to all BB coordinates in $\mathcal{T}_v[k]$, resulting in a new set of stabilized tracks, $\mathcal{T}_v^{\text{ref}}[k]$. We first convert the BBs from the YOLO format (x, y, w, h) into a four-point format representing each box’s corners. Each corner is then transformed using $H_v^{k \rightarrow \text{ref}}$ to align with the reference frame. After transformation, the new positions are converted back into the YOLO format by recalculating the center coordinates and

dimensions, ensuring consistency. This direct application of homography to track data bypasses the need to stabilize the entire video, saving storage space and eliminating artifacts that can obscure parts of the scene, thereby enabling vehicle detection across the entire recorded area. This is a key feature of our work, emphasizing the novelty of stabilizing tracks rather than the video itself.

Furthermore, our masking strategy introduces another key innovation. Unlike conventional methods that warp each video frame to a reference frame before detection and tracking, our approach leverages the detected vehicles to enhance image registration. By applying exclusion masks based on detected BBs, we avoid keypoint matches on moving objects, which can undermine stabilization [103]. This reordering improves accuracy and allows for less stringent hyperparameters without additional computational costs. Our stabilization process is available as the open-source library *stabilo* [31], which supports both video and track stabilization using user-provided masks, and can be seamlessly integrated into various frameworks beyond vehicle tracking.

3.5.2. Method and parameter search campaign

Recent studies [115, 116] suggest that classical image matching algorithms may perform comparably to the perceived SOTA represented by learning-based approaches like SuperPoint or SuperGlue. These findings highlight the importance of careful hyperparameter tuning for classical methods and point out that DL-based methods rely heavily on large training datasets and require fine-tuning for specific tasks. Due to the lack of extensive ground truth image matches in our context, we opted for classical methods to implement the track stabilization routine described above. Classical methods offer a robust solution, often requiring fewer computational resources and no extensive training datasets, making them ideal for our experimental conditions.

To systematically validate and refine our selection of classical algorithms and hyperparameters, we utilized 29 unique aerial scenes \mathcal{S} , each representing a randomly selected frame from our fleet of 10 drones monitoring 20 intersections. With multiple drones covering some intersections, this compilation ensures a diverse array of viewpoints, totaling $|\mathcal{S}| = 29$ distinct scenes similar to those shown in [Fig. 1](#) (right).

For each method and hyperparameter combination, we performed a comprehensive evaluation using all scenes. Each scene was subject to $N_t = 100$ trials involving both photometric and homographic distortions, amounting to 2,900 evaluations per combination. Photometric distortions include brightness variations of up to $\pm 25\%$, Gaussian blur with kernel sizes of up to 5 pixels, saturation adjustments within $\pm 5\%$, and fog effects with an intensity of up to 10%. These distortions simulate various lighting conditions, weather scenarios, and camera focus variations to challenge the robustness of feature detection and matching algorithms. We then applied random homography transformations $H_s^{i \rightarrow i'}$ to each scene $s \in \mathcal{S}$. These transformations, designed to mimic drone movements and environmental effects like wind gust or altitude changes, included rotations up to ± 15 degrees, translations up to $\pm 10\%$ on both axes, scale changes up to $\pm 5\%$, and perspective shifts with coefficients up to 5×10^{-5} to represent subtle changes in drone pitch or roll.

Using image pairs of original and distorted scenes, we applied the image registration techniques discussed earlier to estimate the homography matrix $\hat{H}_s^{i' \rightarrow i}$, using $H_s^{i \rightarrow i'}$ as the ground truth. Comparing the estimated transformations against the actual ones ensures that our algorithms can robustly handle and correct the dynamic transformations typically encountered by drones in real-world scenarios. [Fig. 6](#) provides an overview of our experimental setup, highlighting the rigor of our testing environment tailored for drone video analysis under varying and challenging conditions.

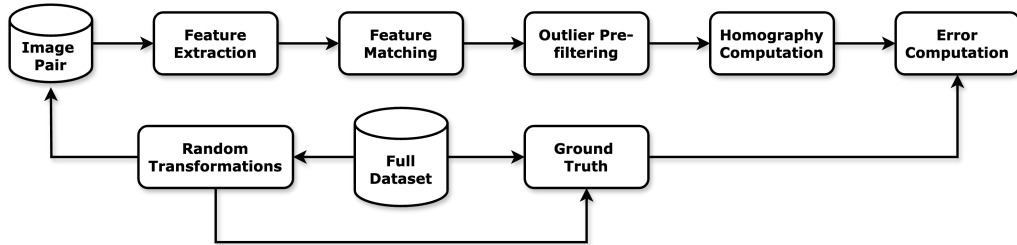


Figure 6: Overview of the image registration campaign.

We implemented several prominent local feature detectors including SIFT, RSIFT, BRISK, ORB, KAZE, and A-KAZE, along with various RANSAC implementations such as the original RANSAC algorithm, MAGSAC++, GC-RANSAC, DEGENSAC, etc. Both BF and FLANN matchers were evaluated, with the options to use exclusion masks and apply CLAHE. We conducted extensive grid searches to optimize parameters such as the SNN ratio threshold (θ_{SNN}), the maximal number of extracted keypoints (K and K_{ref}), the downsample ratio (ρ), and the epipolar threshold

(η) , aiming to balance accuracy and computational efficiency. Following recommendations from recent studies [115], we fixed τ at 0.999999 due to its minimal sensitivity to changes and set the maximum number of iterations Γ at 5,000 for all RANSAC algorithms to ensure sufficient convergence. Finally, we opted for unidirectional matching, avoiding bidirectional approaches to reduce computational demands.

Traditionally, the mean Average Accuracy (mAA) metric is used to evaluate the effectiveness of image registration. However, this requires knowledge of the camera intrinsics and computation of the essential matrix. Alternatively, homography estimation accuracy (HEA) is a widely used metric [116] for image registration evaluation, defined as:

$$\text{HEA} = \frac{1}{N_t \times |\mathcal{S}|} \sum_{s \in \mathcal{S}} \sum_{i=1}^{N_t} \begin{cases} 1, & \text{if } \left(\frac{1}{|\mathcal{P}|} \sum_{p \in \mathcal{P}} \left\| p - \hat{H}_s^{i' \rightarrow i} (H_s^{i \rightarrow i'}(p)) \right\| \right) \leq \varepsilon \\ 0, & \text{otherwise} \end{cases}. \quad (6)$$

This equation calculates the average accuracy across all transformations for each scene, where each corner's displacement after a round-trip transformation through the true homography H and its estimation \hat{H} is computed. The set \mathcal{P} contains the 2D coordinates of the four corner points of the original scene, and $H(\cdot)$ or $\hat{H}(\cdot)$ represent the homography transformation of a 2D point as described in (4) and (5). If the average displacement is within a threshold ε , it contributes a ‘1’ (accurate) to the average; otherwise, it contributes a ‘0’.

Although HEA is useful, it alone may not suffice for our traffic analysis purposes. Accurately matching the four corner points of a scene does not necessarily ensure that visible objects, such as vehicles, are correctly represented after transformation. Therefore, we introduce a new traffic-oriented metric denoted here as mean IoU (MIoU), which leverages the IoU of the re-projected vehicle BBs:

$$\text{MIoU} = \frac{1}{N_t \times |\mathcal{S}|} \sum_{s \in \mathcal{S}} \sum_{i=1}^{N_t} \left(\frac{1}{|\mathcal{B}_s|} \sum_{B \in \mathcal{B}_s} \frac{B \cap \hat{H}_s^{i' \rightarrow i} (H_s^{i \rightarrow i'}(B))}{B \cup \hat{H}_s^{i' \rightarrow i} (H_s^{i \rightarrow i'}(B))} \right). \quad (7)$$

This equation measures the average IoU for BBs across all scenes and transformations, where \mathcal{B}_s denotes the set of BBs in scene $s \in \mathcal{S}$. It computes the IoU between each original BB B and its transformed version after applying the true and estimated homographies. The advantage of this metric is that it does not require a pixel threshold and yields values ranging from 0 to 1, making it suitable for our application and valuable addition to HEA.

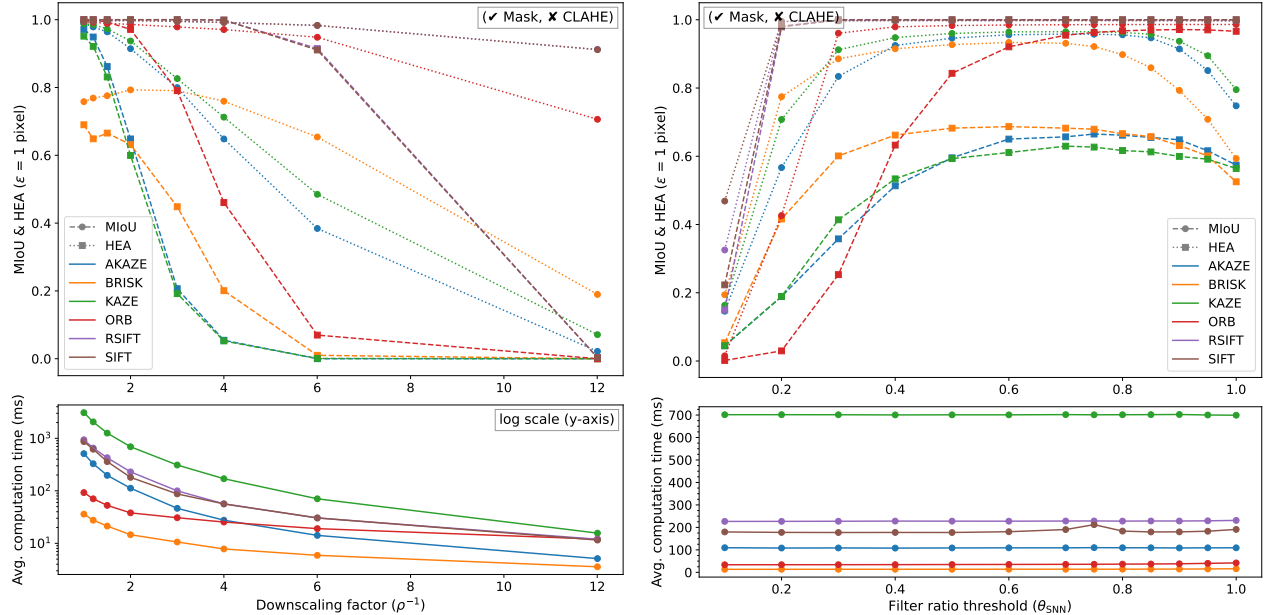


Figure 7: Effect of downscaling ratio and SNN filter ratio threshold on the image registration performance¹.

¹All computational timings were obtained on a system equipped with an Intel Core i9-13900KF processor, NVIDIA GeForce RTX 3090 graphics card, and 64GB of RAM, operating on Ubuntu 22.04.3 LTS.

While a detailed presentation of our campaign results is beyond the scope of this paper, we will make our software tool publicly available [32] to enable replication and adaptation of our methods and hyperparameters for similar image registration tasks. [Fig. 7](#) offers insights into the optimization process, particularly highlighting the impact of downscaling and SNN threshold on image registration performance.

Ultimately, our findings suggest the following optimal set of methods and parameters: an ORB detector with $K = 2,000$ and $K_{\text{ref}} = 4,000$, a BF feature matcher with $\theta_{\text{SNN}} = 0.9$, and MAGSAC++ with $\tau = 0.999999$, $\Gamma = 5,000$, and $\eta = 2$, coupled with downscaling by a factor of $\rho = 0.5$ and the use of BBs with $\epsilon = 0.15$ as exclusion masks. The use of CLAHE did not provide any significant benefits. Except for θ_{SNN} or ρ , these parameters were fixed for the trials producing [Fig. 7](#).

As shown in [Fig. 7](#), the selected combination of methods and parameters, particularly ORB with a downscaling factor of $\rho = 0.5$, achieves high MIoU and HEA values. This performance is on par with leading results reported in image matching studies [115, 116] and effectively balances superior accuracy with the computational efficiency required to process our extensive 12TB of video data.

[Fig. 8](#) demonstrates the image matching between the reference (first) frame and the last ($N_v = 4,679$) frame of an example video v lasting approximately 2 minutes and 36 seconds. Out of 1,773 matched keypoints passing the SNN threshold, 673 inliers were used for computing $H_v^{N_v \rightarrow \text{ref}}$, while MAGSAC++ rejected the remaining 1,100 as outliers. Notably, all matched keypoints lie outside the provided exclusion masks, which cover the detected vehicles. Unlike the rejected matches, the inlier lines exhibit consistent directionality, indicating a robust subset for accurate homography estimation.

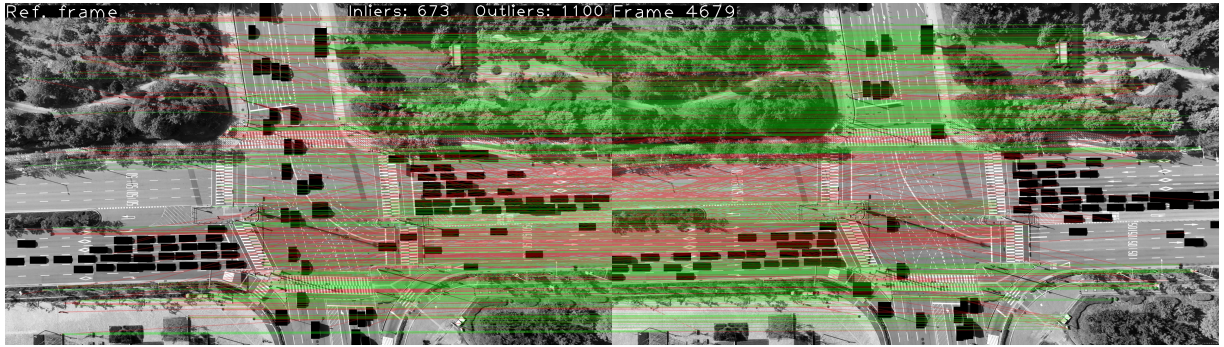


Figure 8: Image matching between the reference frame and the last frame of a video. Green lines indicate inliers used for homography computation, while red lines represent outliers rejected by the MAGSAC++ algorithm. Exclusion masks effectively prevent keypoint detection in vehicle regions.

3.6. Georeferencing

3.6.1. Orthophoto creation and road segmentation

In our study, a detailed orthophoto encompassing all 20 monitored intersections within the Songdo experimental area was produced, as shown in [Fig. 9](#) (left). This was achieved using a dedicated DJI Mavic 2 Pro drone flying at an altitude of 75 meters, capturing overlapping high-resolution ($6,000 \times 4,000$ pixels) and distortion-free imagery that was then meticulously stitched using sophisticated photogrammetry methods facilitated by Dromii's in-house Drone as a Service (DaaS) platform². The drone captured images over the course of several days during the experiment and on additional dates to further enhance the final orthophoto.

The geospatial accuracy of the orthophoto was significantly enhanced using 13 GCPs, each marked with a 1×1 meter QR code and strategically placed across the experimental area, see [Fig. 9](#) (left). These GCPs were calibrated using an EMLID RS2+ multi-band RTK-GNSS receiver, featuring multi-feed antennas for multipath rejection and a fast RTK convergence. According to the manufacturer, this rover can reliably ensure geolocation accuracy up to 8 km from the base station. The final orthophoto boasts a resolution of $209,181 \times 181,692$ pixels and a file size exceeding 30GB, providing an unprecedented level of detail.

For focused traffic analysis, $15,000 \times 15,000$ pixel cut-outs centered on each intersection were first extracted from the large orthophoto, as shown in [Fig. 9](#) (right) for one example. These cut-outs sufficiently cover areas our drones monitor and are instrumental for in-depth traffic analysis and visualizations. DL-based techniques were integrated into

²<http://new.dromii.com/>

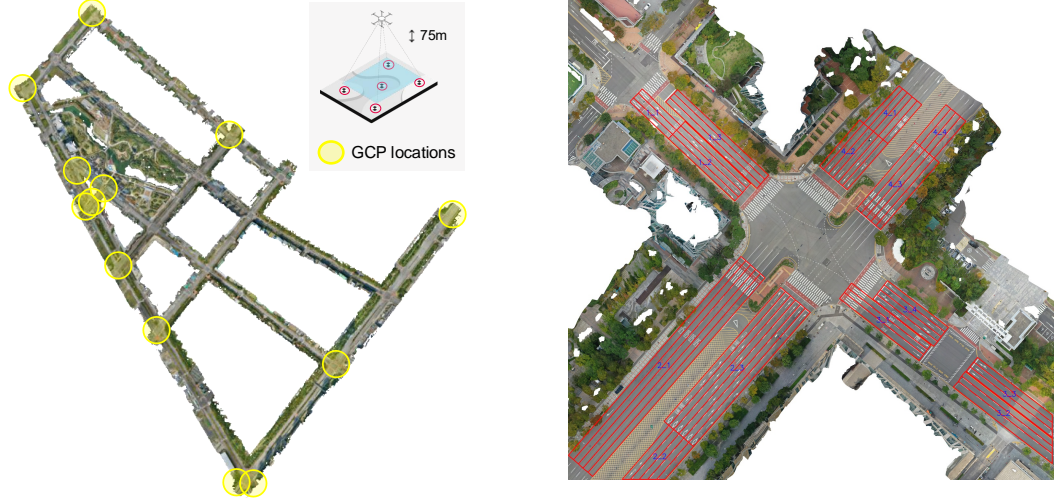


Figure 9: Left: Orthophoto encompassing all 20 monitored intersections, showing the locations of the GCPs used during its creation. Right: Example of an orthophoto cut-out for a specific intersection, with overlaid road section and lane segmentations.

the photogrammetry process to exclude vehicles from the imagery, ensuring that the orthophoto is devoid of transient obstructions such as cars. Tall objects such as buildings were also removed during the orthophoto creation process. These exclusions do not impede the georeferencing step, discussed in [Section 3.6.2](#), as there are still ample areas for extracting enough feature points. More importantly, our primary goal for accurate georeferencing is to ensure feature correspondences at the road level.

Each of the 20 cut-outs underwent manual segmentation to delineate road sections and lanes, as illustrated in [Fig. 9](#) (right). In this context, sections refer to areas that group lanes moving in the same direction within defined parts of the intersection. Each section is labeled as "N_G," where N designates the specific node of the intersection, and G represents the grouping of lanes by direction and number. Lanes within each section are numbered sequentially from the innermost lane outward.

These segmentations enabled us to link each trajectory point with a specific road section and lane number, enhancing the dataset's utility. If a vehicle is outside the segmented area (e.g., in the intersection center), no road or lane number is assigned. Additionally, due to perspective, vehicles with significant heights, such as trucks or buses, may have their centers fall outside the assigned section or lane, leading to potential mislabeling. This metadata is invaluable for analyzing traffic flows at intersections. The segmented orthophotos, along with the trajectories in orthophoto coordinates, will be included in the public Songdo Traffic dataset.

3.6.2. Trajectory georeferencing

The main goal of georeferencing is to transform the vehicle trajectories in $\mathcal{T}_v^{\text{ref}}[k]$ into real-world coordinates, such as longitude and latitude. This process, illustrated in [Fig. 10](#), utilizes a three-step transformation, with the first two steps similar to the method used in track stabilization.

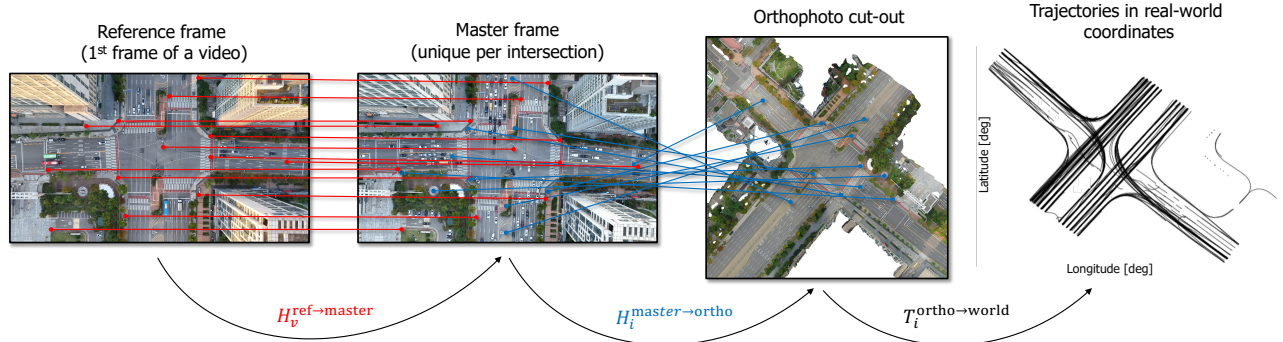


Figure 10: Illustration of the steps involved in the georeferencing process.

Step 1: For each video v , we calculate a homography matrix $H_v^{\text{ref} \rightarrow \text{master}}$, which maps the stabilized tracks from the reference frame F_v^{ref} to a “master frame”. Each monitored intersection i has its own unique master frame, F_i^{master} , serving as a unified basis to ensure consistent alignment across all videos capturing the same location.

Step 2: Next, a homography matrix $H_i^{\text{master} \rightarrow \text{ortho}}$ is computed to transition these coordinates from the master frame to the orthophoto coordinates F_i^{ortho} . Here, F_i^{ortho} is the orthophoto cut-out corresponding to intersection i . The complete transformation from the video’s reference frame to the orthophoto coordinates is expressed as:

$$H_v^{\text{ref} \rightarrow \text{ortho}} = H_i^{\text{master} \rightarrow \text{ortho}} \cdot H_v^{\text{ref} \rightarrow \text{master}}. \quad (8)$$

This composite homography $H_v^{\text{ref} \rightarrow \text{ortho}}$ allows us to map any point p_v^{ref} in the reference frame F_v^{ref} directly to its corresponding point p_i^{ortho} in the orthophoto F_i^{ortho} , i.e., $p_i^{\text{ortho}} = H_v^{\text{ref} \rightarrow \text{ortho}}(p_v^{\text{ref}})$. Applying this transformation to all stabilized vehicle coordinates in $\mathcal{T}_v^{\text{ref}}[k]$, we obtain the vehicle trajectories in the orthophoto CS.

Step 3: The transformation from orthophoto coordinates to real-world geographic coordinates is executed using a 2×3 affine transformation matrix $T_i^{\text{ortho} \rightarrow \text{world}}$. This matrix employs six georeferencing parameters embedded in the orthophoto, enabling the accurate conversion of pixel coordinates to geographic coordinates. This transformation is typically expressed by the following affine equations:

$$\begin{aligned} \phi &= a_i \cdot x_{\text{ortho}} + b_i \cdot y_{\text{ortho}} + t_{x_i}, \\ \lambda &= c_i \cdot x_{\text{ortho}} + d_i \cdot y_{\text{ortho}} + t_{y_i}, \end{aligned} \quad (9)$$

where x_{ortho} and y_{ortho} are the pixel coordinates in the orthophoto, and $a_i, b_i, c_i, d_i, t_{x_i}$, and t_{y_i} are the parameters that form the matrix $T_i^{\text{ortho} \rightarrow \text{world}}$, derived from the i -th orthophoto’s metadata. These parameters account for the scale, rotation, and translation adjustments necessary to map the pixel coordinates to the real-world coordinates ϕ (latitude) and λ (longitude).

By systematically applying these three steps, we ensure that all vehicle center coordinates $(x^{(i)}[k], y^{(i)}[k])$ in $\mathcal{T}_v^{\text{ref}}[k]$ are accurately mapped to real-world locations. This precise georeferencing enables seamless integration with other spatial data. To facilitate this, we converted all stabilized trajectories in $\mathcal{T}_v^{\text{ref}}[k]$ into both the global geographic CS (latitude and longitude, EPSG:4326, also known as WGS84) and the local Cartesian CS (X and Y, EPSG:5186). Both these converted trajectories will be included in our dataset.

Simpler georeferencing methods, such as those based on GSD or traditional GIS software for manual image alignment, may suffice for static deployments. However, as noted in [Section 2.4](#), these approaches often lack the accuracy and efficiency necessary for effective traffic monitoring. Therefore, we employed an orthophoto-based method to achieve the high precision and reliability required for accurate coordinate transformations in our extraction framework.

3.6.3. Optimization of orthophoto cut-out resolution for accurate georeferencing

While the transformation $T_i^{\text{ortho} \rightarrow \text{world}}$ is directly obtained from the orthophoto creation process, the homographies $H_v^{\text{ref} \rightarrow \text{master}}$ and $H_i^{\text{master} \rightarrow \text{ortho}}$ need to be computed using image registration techniques similar to those used in track stabilization. Since these homographies are calculated only once per video and per intersection, respectively, computational efficiency is not a critical concern at this stage. This allows for the use of a superior feature detector, such as RSIFT, which utilizes a square root (Hellinger) kernel to evaluate the similarity of SIFT descriptors, rather than the standard Euclidean distance. Our optimization experiments confirmed that this method enhances performance in all stages of image registration [\[86\]](#). In our implementation, we set the maximum number of feature points to $K = 100,000$, employed a BF matcher with $\theta_{\text{SNN}} = 0.55$, and configured MAGSAC++ with $\tau = 0.999999$, $\Gamma = 10,000$, and $\eta = 3$. Notably, we did not apply CLAHE and found exclusion masks unnecessary, as vehicles present in the reference and master frames differ, and the orthophoto is devoid of vehicles.

To validate the reliability of our georeferencing process, we conducted a comprehensive evaluation to determine the optimal resolution for orthophoto cut-outs. While the 4K reference and master frames were used at their full resolution without downscaling, we performed an ablation study to assess the impact of different resolutions for the orthophoto cut-outs. Specifically, we selected two intersections, L and P. For each intersection, we chose two reference frames, one from a morning and one from an afternoon flight session, to account for varying lighting conditions. We meticulously annotated these frames and the full-sized cut-outs with 10 corresponding GCPs for each frame and cut-out pair, aiming for pixel-level accuracy (see [Fig. 11](#) for illustration). This resulted in a total of 40 GCP correspondences for validation.

For each combination of image frame and orthophoto cut-out, we computed the homography matrix using the aforementioned image registration techniques and parameters. We repeated this process across a range of orthophoto cut-out resolutions. The mean and standard deviation of the pixel reprojection errors were calculated by transforming points from the orthophoto cut-outs back to the image frame and comparing them with the original GCPs in that frame. These errors are summarized in [Table 4](#) for each resolution. Additionally, we report the average computation time, as well as

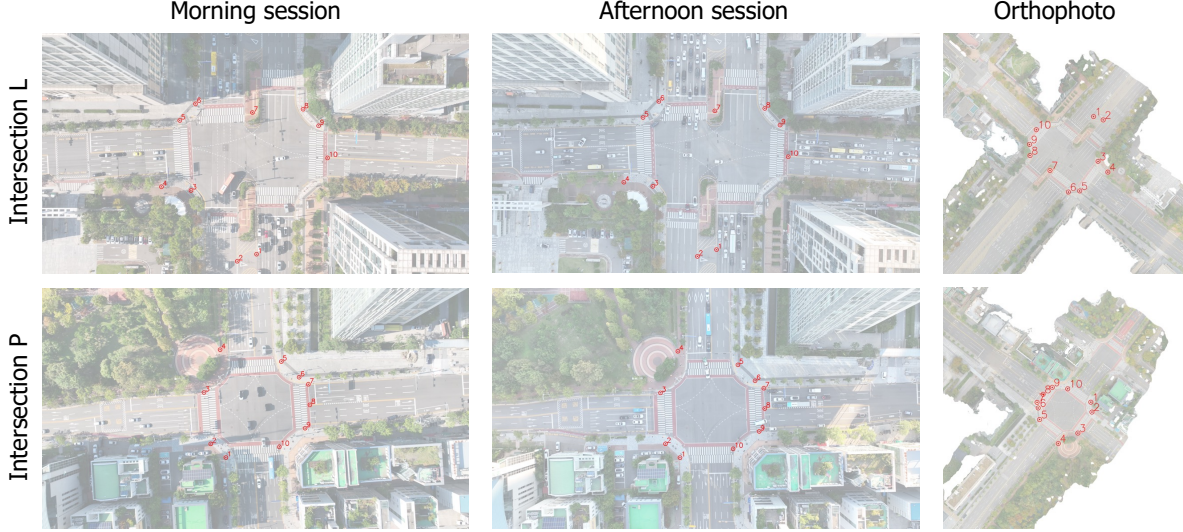


Figure 11: Locations of the GCPs for the selected intersections L and P.

the average and minimum number of inliers after applying MAGSAC++ for outlier rejection. It is important to note that the results may include some degree of human error due to the manual assignment of GCPs. All computations were performed on the same computational infrastructure used for the campaign reported in [Section 3.5.2](#), ensuring consistency in timing measurements.

Table 4: Results of the image matching evaluation between image frames and orthophoto cut-outs at various resolutions.

Cut-out resolution	Average computation time (s)	Reprojection error (px)	Average # of inliers	Minimum # of inliers
2,000	2.576	3.225 ± 2.748	116.75	39
3,000	3.980	1.945 ± 1.357	189.25	62
4,000	9.222	1.671 ± 1.315	258.75	110
5,000	15.552	1.479 ± 1.014	235.5	96
6,000	21.677	1.388 ± 0.957	218.5	104
7,000	23.052	1.469 ± 0.986	189.5	87
8,000	24.854	1.318 ± 0.821	142.75	62
9,000	26.767	1.444 ± 1.155	134.5	66
10,000	28.720	1.419 ± 0.853	111.75	41
11,000	31.575	1.336 ± 0.850	110.0	54
12,000	33.809	1.400 ± 0.989	95.5	40
13,000	36.666	1.514 ± 0.939	94.5	36
14,000	39.578	1.543 ± 1.136	94.0	39
15,000	42.888	1.590 ± 1.013	77.5	30

From the results, we observe that increasing the orthophoto cut-out resolution leads to improved matching accuracy up to a certain point. The reprojection error decreases with higher resolutions, reaching its minimum at 8,000 pixels. There is no improvement beyond this point, while the computational time increases. Additionally, we note that the average number of inliers decreases at higher resolutions. This decrease may be attributed to the increased image detail causing more mismatches and the computational limits of feature matching algorithms at higher resolutions.

Our observations indicate that when the number of inliers falls below approximately 30, the homography estimation becomes unstable. Importantly, at resolutions around 8,000 pixels, the minimum number of inliers remained well above this threshold for all considered intersections and sessions, ensuring reliable homography computation. Based on these findings, we selected a resolution of $8,000 \times 8,000$ pixels as optimal for subsequent processing, as it provided the best matching accuracy in our evaluation. Consequently, we downsampled all orthophoto cut-outs to this resolution. This resolution also facilitated manual segmentation of road sections and lane delineations, resulting in manageable orthophoto

file sizes (approximately 80 ~ 100MB), enhancing dataset usability. With a mean reprojection error below two pixels, our orthophoto registration method demonstrates high accuracy, validating the effectiveness of our georeferencing approach.

3.7. Traffic data

3.7.1. Robust vehicle dimension estimation

Accurate estimation of vehicle dimensions from drone-based video imagery is vital for various traffic analysis applications, yet it remains an underrepresented challenge in scientific literature. To address this gap, we present a novel approach that leverages both un-stabilized and stabilized BBs from sequences $\mathcal{T}_v[k]$ and $\mathcal{T}_v^{\text{ref}}[k]$, respectively. Our unique methodology offers a significant advancement in the field, providing a level of accuracy and robustness previously unattained in similar studies.

Our approach employs a systematic process designed to enhance the robustness and accuracy of vehicle dimension estimates. The methodology focuses on fully visible BBs and vehicle motions parallel to the X or Y axes of the reference frame F_v^{ref} . The process encompasses visibility filtering, initial dimensions computation, azimuth-based filtering, final dimension computation, and real-world conversion. Additionally, we incorporate a solution for stationary vehicles, which is applicable only when these vehicles are aligned with the F_v^{ref} axis. Detailed implementation steps and experiment-specific parameters are provided in [Appendix A](#).

[Figure 12](#) illustrates the BB filtering process, using actual BBs obtained from a sample trajectory. The figure also shows the final dimension estimate, computed as the first quartile of all “accepted” BBs. The right subfigure demonstrates the consistency of detected BBs along quasi-straight trajectories, with only minor inflations due to the permissible azimuth angle tolerance ($\bar{\theta} = 15^\circ$) and deviations in road alignment relative to the reference drone’s orientation.

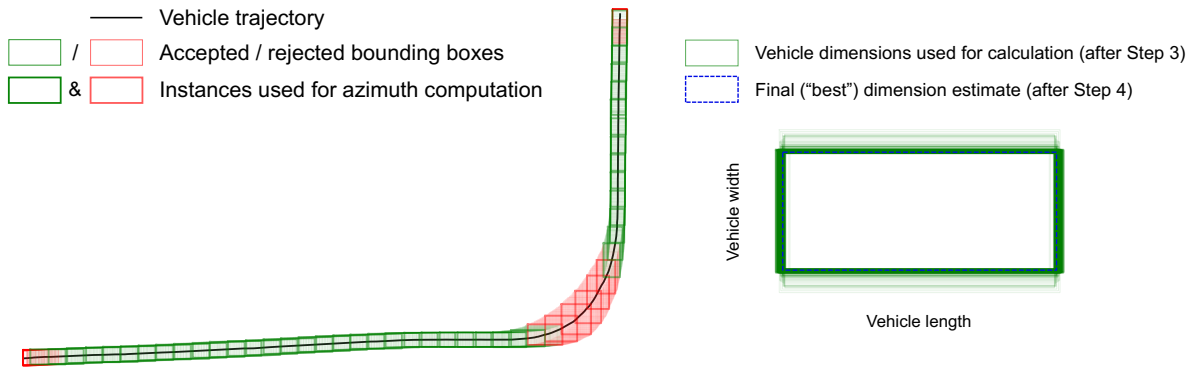


Figure 12: Illustration of the vehicle dimension estimation process for moving vehicles.

It is important to acknowledge certain limitations of our approach. The dimensions derived from BBs in pixel coordinates may slightly overestimate the actual real-world vehicle sizes, often due to the BB encapsulating protruding parts, such as rear-view mirrors, or strong shadows. The method also faces challenges when vehicles travel exclusively on non-parallel roads or remain parked or stationary out of alignment with the image axes. In these cases, as well as when persistent partial occlusions distort the BBs, no dimension estimates are calculated.

Despite these challenges, our approach provides a robust solution for vehicle dimension estimation from drone footage. By addressing the complexities of real-world scenarios and incorporating solutions for both moving and stationary vehicles, this method contributes to advancing the field of traffic analysis in drone-based applications.

3.7.2. Speed and acceleration computation

To maintain the integrity of the extracted trajectories, we refrain from applying smoothing or interpolation techniques, thereby preserving the raw measurement characteristics of the trajectory data. This approach allows users to select the most suitable post-processing methods for their specific needs. However, to facilitate efficient querying of trajectories based on predefined kinematics thresholds, we provide speed and acceleration estimates, which are computed after applying linear interpolation to fill in any potentially missing trajectory points, along with a simple smoothing technique to ensure reliable computation of the speed and acceleration profiles.

We apply a carefully tuned Gaussian filter to smooth the speed data, reducing noise while retaining critical dynamic movement patterns. The tuning process utilized the AV data (see [Section 4.2](#)) to ensure an accurate representation of real-world vehicle motion. The smoothed speed forms a robust basis for precise acceleration computation. The details of

the vehicle kinematics computation and tuning are presented in [Appendix B](#). Our approach allows for future exploration of more advanced methods, such as those employed in [\[117\]](#). The availability of raw trajectory data in our dataset allows users to implement custom filtering techniques, such as the Kalman filter [\[67\]](#) or the Rauch-Tung-Striebel (RTS) smoother [\[118\]](#), tailored to their specific needs and applications.

3.7.3. Construction of the Songdo Traffic dataset

The Songdo Traffic dataset is compiled from data collected by 10 drones monitoring 20 intersections over four days, encompassing approximately 1 million unique vehicle trajectories. These trajectories are preserved at the original camera capture rate of approximately 30 FPS, ensuring high-resolution data without down-sampling. The extraction and processing of vehicle trajectories is conducted on a per-video basis. As described in [Section 3.1](#), the video segmentation methodology associates each video with a specific day, flight session, intersection, drone, and hovering sequence, resulting in the creation of over 3,000 individual comma-separated values (CSV) files. Detailed column descriptions of these files are provided in [Table 5](#).

Table 5: Column descriptions for the Songdo Traffic dataset. Note: Entries separated with '/' indicate separate columns.

Dataset column name	Explanation
Vehicle ID	Unique identifier assigned to each tracked vehicle (integer: 1, 2, ...)
Drone ID	Unique identifier for the drone capturing the data (integer: 1, 2, ...)
Local date and time	Local Korean date and time (GMT+9) in ISO 8601 format ("YYYY-MM-DD hh:mm:ss.sss")
Ortho X / Y	Pixel coordinates of vehicle center in orthophoto cut-out image space
Local X / Y	Planar coordinates (meters) of vehicle center in KGD2002 / Central Belt 2010 (EPSG:5186)
Latitude / Longitude	Geographic coordinates (degrees) of vehicle center in WGS84 (EPSG:4326)
Vehicle length / width*	Estimated length and width of vehicle (meters)
Vehicle class	Vehicle type categorization: 0 (car, van, or light-duty vehicle), 1 (bus), 2 (truck), 3 (motorcycle)
Vehicle speed / acceleration*	Derived instantaneous speed (km/h) / acceleration (m/s ²) of the vehicle
Road section ID*	Identifier for road section (N.G format, where N = node, G = lane group) at vehicle's location
Lane number*	Current lane position of vehicle (1 = leftmost lane in road section)
Visibility	Boolean flag indicating full visibility of vehicle in image frame (1 = visible, 0 = partially visible)

* These fields may be empty under certain conditions (see [Section 3.6.1](#), [Section 3.7.1](#), [Section 3.7.2](#)).

To efficiently manage the large number of files, trajectories are aggregated per individual intersection and flight session basis, with file names reflecting the corresponding intersection and session. The aggregated files from each of the 10 daily flight sessions are packaged into 80 ZIP files, each containing traffic data for a specific intersection and day of the experiment. Additionally, the Songdo Traffic dataset includes 20 orthophoto cut-outs with road and lane segmentation overlays. This arrangement ensures the full usability of the trajectory data in orthomap coordinates, enabling a holistic analysis of traffic dynamics and environmental interactions.

4. Results

4.1. Traffic data extraction

We present key characteristics and the potential of georeferenced trajectories extracted using our complete methodology. We focus on the final day of the experiment, Friday, which represents one of the most congested periods. Specifically, we examine intersection L, illustrated in [Fig. 13](#) (left), where the horizontal road has a speed limit of 30 km/h and the vertical road has a speed limit of 50 km/h, and was monitored by drone 7 (D7) flying at 150 m during the final afternoon session (PM5), which commenced at 17:40.

This session yielded four videos ($v \in L1, L2, L3, L4$) with a combined duration of approximately 6 minutes and 55 seconds, from which we extracted trajectories of various lengths representing 1,194 unique vehicles. The effectiveness of our detection and tracking is illustrated in [Fig. 13](#) (left). Color-coded BBs indicate precise identification and classification of vehicles: blue for cars, red for buses, orange for trucks, and green for motorcycles. The trailing tails, representing the last second of vehicle movement, highlight vehicle dynamics such as speed and stopping behavior.

As shown in [Fig. 13](#) (right), the aggregated trajectories in the local CS captured by D7 during PM5 demonstrate our framework's ability to process end-to-end from raw videos to consistent georeferenced trajectories. This visualization underscores the framework's effectiveness in analyzing dynamic traffic flows within congested urban settings and highlights the significant contributions of our Songdo Traffic dataset in providing immersive insights into urban mobility.

Unlike previous UAV-based extraction methodologies, our approach yields realistic acceleration and speed distributions, as shown in [Fig. 14](#) (left). Speed values are filtered to exclude those below 1 km/h for better plot legibility. The corresponding vehicle class distribution is shown in [Fig. 14](#) (right). Notably, the speed distributions resemble realistic

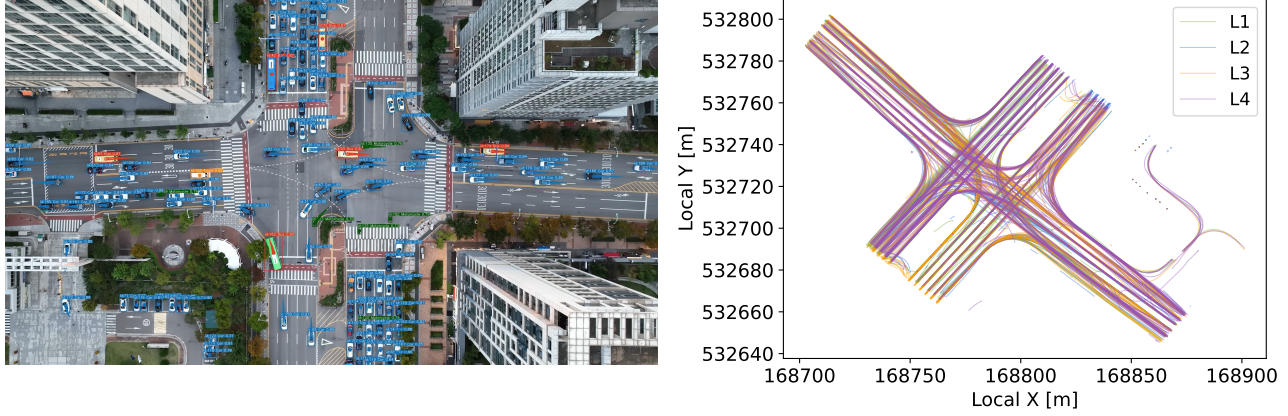


Figure 13: Left: Vehicle detection and tracking illustration. Right: Aggregated trajectories in local CS.

patterns for an intersection with 30 km/h and 50 km/h road limits, however, the significant congestion during this period results in limited probability mass near the 50 km/h mark. Additionally, the acceleration distributions align closely with those reported in fixed camera setups [117], reflecting the effectiveness of our track stabilization. In contrast, previous UAV-based trajectory extraction methods often exhibit large and unrealistic acceleration variances with heavy tails, often reaching up to $\pm 300 \text{ m/s}^2$, mainly due to camera shakiness and inadequate video stabilization [117].

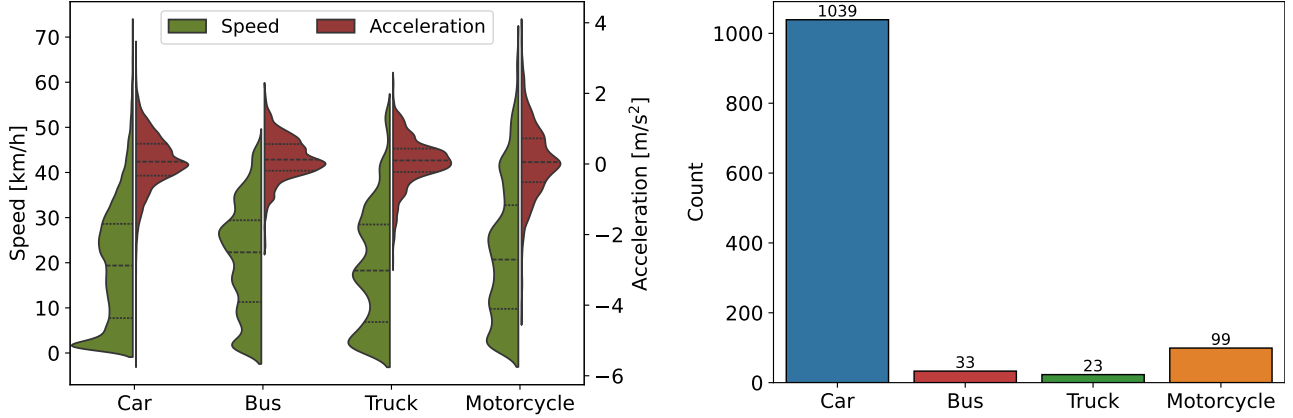


Figure 14: Left: Vehicle speed and acceleration distributions. Right: Vehicle class distribution.

The estimated vehicle dimensions are depicted in Fig. 15, which shows the length and width distributions for different vehicle classes. Notably, the median length and width for the car category are approximately 4.9 m and 2.1 m, respectively, which align closely with average vehicle dimensions reported in previous studies. For example, a study on passenger car external dimensions found that the average length of sedans is 5.1 m and the average width is 1.89 m, while SUVs have an average length of 4.95 m and an average width of 1.94 m [119]. The significant differences in length and width between buses and motorcycles also demonstrate the effectiveness of our dimension estimation approach.

To further validate our dimension estimation approach, we leveraged the AV experiment, which is detailed in Section 4.2. The AV used in this experiment is a Hyundai IONIQ 5 compact crossover SUV, with known dimensions of 4.635 m in length and 1.890 m in width (2.116 m with side-view mirrors). Its distinctive Stanford logo made it easily identifiable in our drone footage. Our estimates, based on 15 video observations (see Fig. 18), yielded a length distribution of $4.931 \pm 0.225 \text{ m}$ and a width distribution of $2.15 \pm 0.072 \text{ m}$. While the width estimate is relatively accurate, length estimates were often inflated due to strong shadows present in the majority of videos. This is confirmed by the lower quartile of the length distribution (4.685 m), which is closer to the ground truth value (4.635 m).

We also conducted a similar analysis using a public transportation bus, specifically a Hyundai Super AeroCity model year 2018, which was easily identifiable in the drone footage due to its distinct color and shape. The bus, depicted in Fig. 13 (blue bus, top-center), has known dimensions of $10.955 \times 2.490 \text{ m}$ (excluding wing mirrors). From 12 videos, 6 from morning and 6 from afternoon sessions, captured at 2 intersections, we extracted 20 distinct instances of this bus and estimated their dimensions. Our results showed a length distribution of $11.540 \pm 0.227 \text{ m}$ and a width distribution

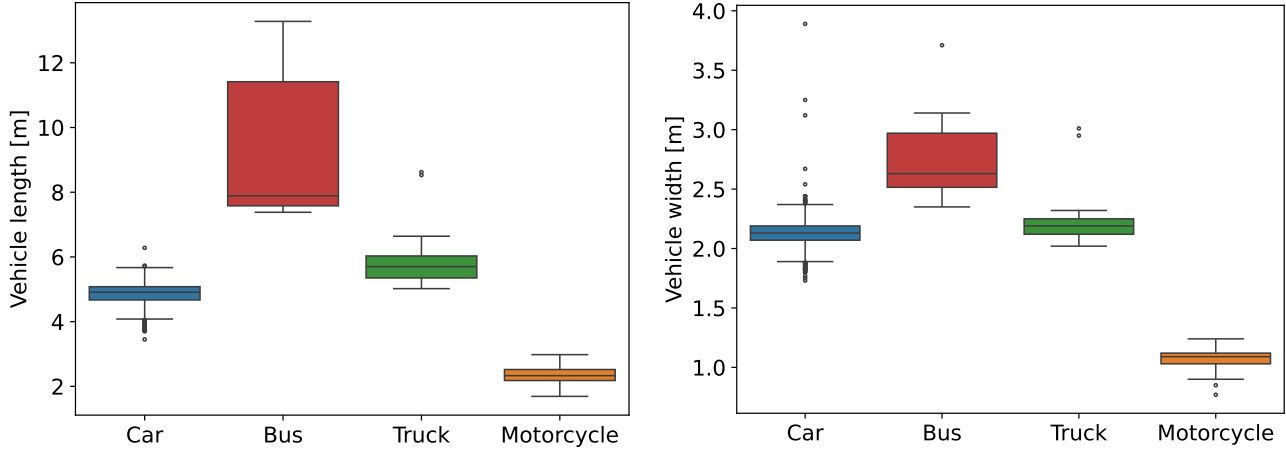


Figure 15: Estimated vehicle length and width distributions.

of 3.063 ± 0.179 m, indicating that the estimates were slightly inflated due to the bus's protruding mirrors, shadows, and height-related perspective distortions. The wing mirrors, each 21 cm wide, likely contribute to the width discrepancy, bringing the total width to approximately 2.910 m, closer to our estimated width distribution.

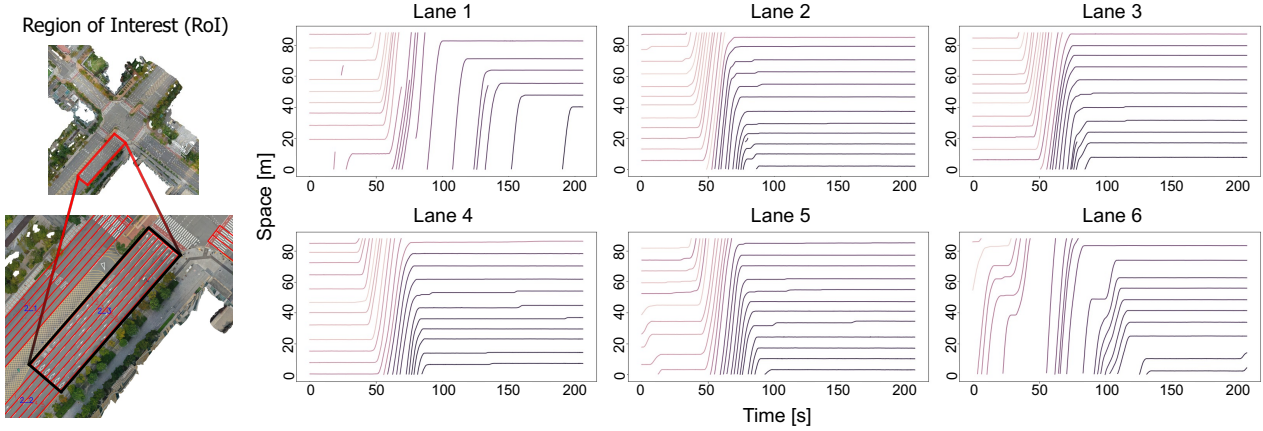


Figure 16: spatio-temporal diagram example for intersection L, road segment 2_3 and lanes 1–6 within the depicted region of interest (RoI).

The spatio-temporal diagram in Fig. 16 visualizes traffic flow dynamics at intersection L, highlighting the temporal progression of vehicle movements and queue formation and dissipation across six lanes. To maintain legibility, the diagram shows trajectories from a single video. Notable patterns include distinct queue buildup and clearance in the left-turn lane (Lane 1), consistent flow in straight-ahead lanes (Lanes 2-5), and dynamic stop-and-go behavior in the right-turn lane (Lane 6). Shorter trajectories, particularly in Lanes 1 and 2, correspond to motorcycles changing lanes or exiting the road section, causing intermittent traffic patterns. The inclusion of road section and lane-level information in our dataset enables users to create similar spatio-temporal analyses, facilitating granular studies of traffic behavior that are often limited by other datasets.

4.2. Comparison with RTK-GNSS data from the probe AV

To assess the reliability of our extraction framework, we compared the drone-derived trajectories and speed profiles with those recorded by the RTK-GNSS sensor on the AV. Conducted by Stanford University, the AV experiment coincided with our monitoring campaign, providing a unique validation opportunity. This comparison allowed us to evaluate the accuracy of our framework against an independent measurement source (see Fig. 17, left).

The AV experiment commenced at 8:53:38 AM on the final day of our monitoring campaign and lasted approximately 1 hour and 10 minutes. Fig. 17 (right) shows the AV's full trajectory and speed profile. Given the dynamic nature of our drone operations, which alternated over multiple intersections during each flight session, our analysis here focuses

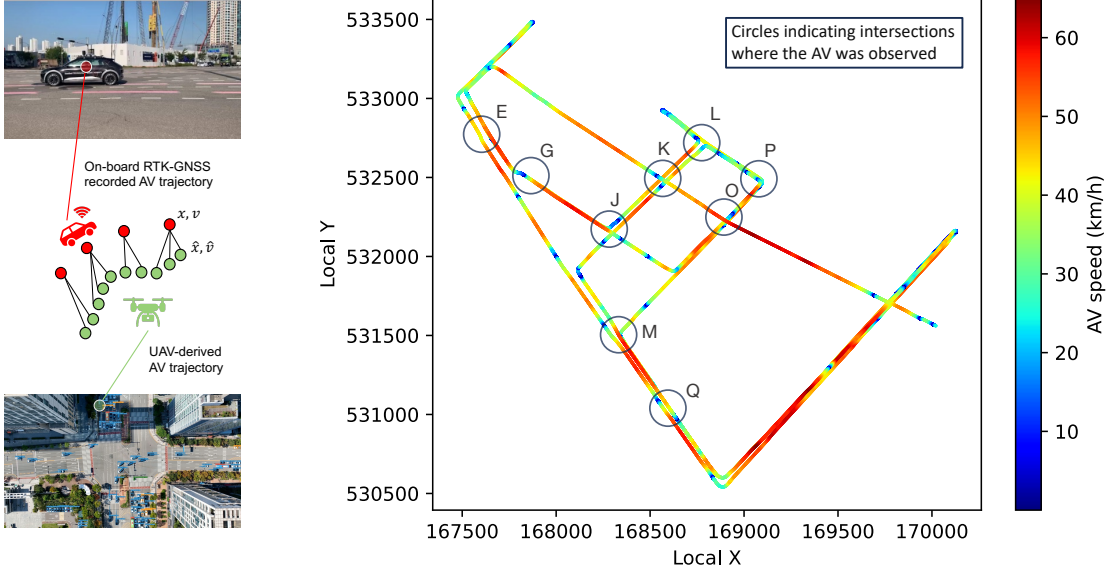
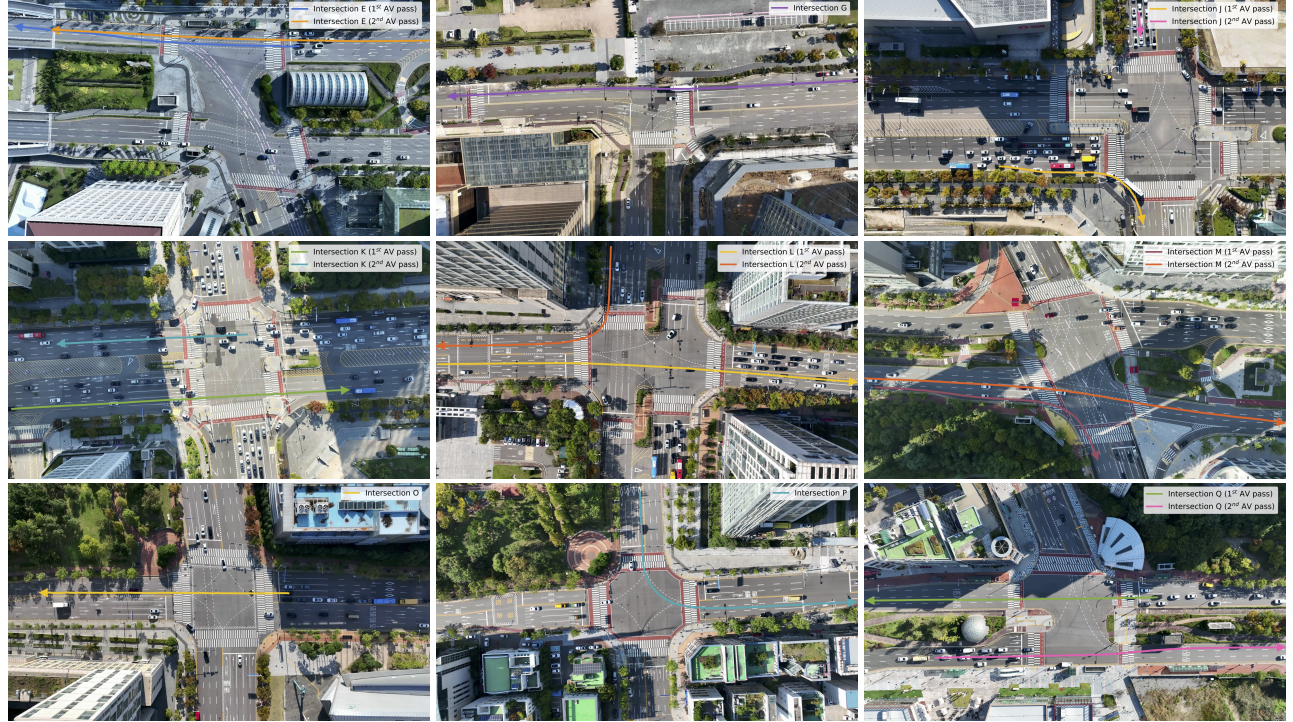


Figure 17: Left: Illustration of the two AV trajectory measuring principles. Right: On-board RTK-GNSS recorded AV trajectory converted to local CS, with marked intersections where our drones recorded the AV passing.

exclusively on static hoverings above intersections. Consequently, we observed the AV at nine intersections (see Fig. 17), recording a total of fifteen distinct AV passes, as illustrated in Fig. 18.



Unfortunately, the timestamps of the AV trajectory from the RTK-GNSS sensor are not synchronized with our UAVs' internal clocks. Additionally, the RTK-GNSS data is asynchronously sampled and undersampled, averaging 10 Hz, while our trajectories are extracted at a fixed 29.97 FPS rate. Due to these differences, we use separate time indices: k_1 for the RTK-GNSS data and k_2 for our UAV-derived trajectory. This discrepancy makes direct Euclidean distance comparisons infeasible, necessitating a more suitable error measurement method [120].

In our methodology, we calculate the positional deviations between the two trajectories in the local CS by measuring the distance $d_P[k_1] \geq 0$. This distance represents the perpendicular separation from the RTK-GNSS trajectory point $P[k_1] = (x_L[k_1], y_L[k_1])$ to the line defined by the two closest trajectory points from our UAV-derived data. For a visual illustration of this computation, see [Fig. 19](#).

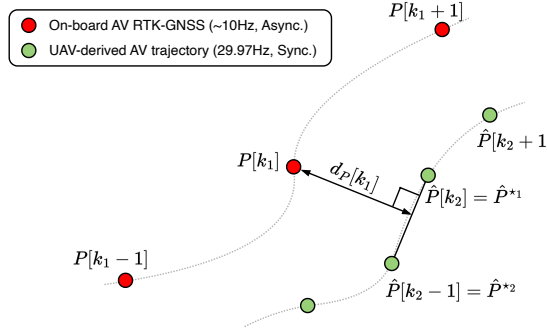


Figure 19: Illustration of positional deviation determination between RTK-GNSS data point and UAV-derived trajectory.

The absolute positional deviation $d_P[k_1]$ at discrete time k_1 is computed as follows:

$$d_P[k_1] = \left| \frac{(\hat{P}^{\star_2} - \hat{P}^{\star_1}) \times (\hat{P}^{\star_1} - P[k_1])}{\|\hat{P}^{\star_2} - \hat{P}^{\star_1}\|} \right|, \quad (10)$$

where ' \times ' denotes the cross product. Here, \hat{P}^{\star_1} is the point on the UAV-derived trajectory that is closest to $P[k_1]$, and \hat{P}^{\star_2} is the adjacent point to with the second shortest Euclidean distance to $P[k_1]$.

In a similar manner, we compute the speed difference $\Delta v[k_1]$ at k_1 as follows:

$$\Delta v[k_1] = v[k_1] - (w^{\star_1} \tilde{v}^{\star_1} + w^{\star_2} \tilde{v}^{\star_2}), \quad (11)$$

where \tilde{v}^{\star_i} is the smoothed speed estimate associated with \hat{P}^{\star_i} . The weights $0 \leq w^{\star_i} \leq 1$ are given by: $w^{\star_1} = d^{\star_1}/(d^{\star_1} + d^{\star_2})$ and $w^{\star_2} = d^{\star_2}/(d^{\star_1} + d^{\star_2})$, where $d^{\star_1} = \|\hat{P}^{\star_1} - P[k_1]\|$ and $d^{\star_2} = \|\hat{P}^{\star_2} - P[k_1]\|$ are the Euclidean distances between the on-board measurement $P[k_1]$ and the UAV-derived points \hat{P}^{\star_1} and \hat{P}^{\star_2} , respectively.

We applied the above methodology to compute d_P and Δv for each of the captured AV passes (illustrated in [Fig. 18](#)). To ensure accurate calculations, we segmented the AV videos to exclude any initial or final stationary periods, such that the start and end of each video segment capture the AV in motion. Additionally, we filtered out speed difference values from $\Delta v[k_1]$ that corresponded to $v[k_1] \leq 1$ to prevent bias in our results. Finally, we aggregated the computed differences for each intersection to facilitate a clear and concise presentation of our findings.

The comparison results are summarized in [Table 6](#). Overall, the UAV-derived trajectories show strong agreement with RTK-GNSS measurements, with average positional deviations remaining below 1 meter at most intersections, except for L and P. Similarly, speed differences between the two methods are minimal, averaging within ± 1 km/h, except at intersection M, where a larger discrepancy likely reflects the high speed variability observed during both AV passes. However, it is important to note that neither measurement method can be considered as an absolute ground truth. The observed discrepancies may stem from differences in the measurement methodologies. Specifically, the location of the on-board RTK-GNSS sensor may not coincide perfectly with the vehicle center derived from the BBs in our UAV footage. Additionally, there could be cumulative effects of small inaccuracies in BB detection, object tracking, track stabilization, and georeferencing. Despite these potential sources of error, the high consistency between the two measurement methods strengthens confidence in the reliability of the Songdo Traffic dataset's extracted trajectories and speed estimates.

To investigate the elevated positional discrepancies at intersections L and P, we generated locally rectified experimental orthophotos using enhanced georeferencing techniques. These orthophotos were intended to examine and potentially rule out any inaccuracies in the original orthophoto. A DJI MAVIC 3 drone was employed to capture high-resolution, overlapping images from an altitude of 75 m. To ensure higher geospatial accuracy, four GCPs were strategically placed at each corner of intersections L and P, each marked with a 3×3 meter QR code. These GCPs were precisely positioned using dual EMLID RS2+ RTK-GNSS receivers operating in FIX mode, providing centimeter-level accuracy, in contrast

Table 6: Comparison of positional and speed differences (mean \pm standard deviation) between drone-extracted trajectories and on-board RTK-GNSS measurements of the AV, along with aggregated trajectory statistics (length and duration).

Intersection label	Positional deviation (m)	Speed difference (km/h)	Trajectory length (m)	Trajectory duration (s)
E	0.476 ± 0.350	-0.403 ± 1.464	334.89	26.49
G	0.289 ± 0.086	-0.518 ± 0.742	190.41	15.70
J	0.493 ± 0.248	0.859 ± 1.351	99.78	20.20
K	0.366 ± 0.198	-0.141 ± 0.508	266.16	21.81
L	1.883 ± 0.334	-0.131 ± 0.906	332.20	35.41
M	0.519 ± 0.614	-1.104 ± 2.893	334.37	49.88
O	0.606 ± 0.141	-0.919 ± 1.162	123.52	14.40
P	1.129 ± 1.247	-0.529 ± 2.400	151.97	38.71
Q	0.359 ± 0.238	-0.144 ± 1.536	322.18	33.20

to the less precise SINGLE mode. The experimental orthophotos were then generated using Agisoft Metashape Pro software³, leveraging the improved accuracy and increased number of GCPs.

These newly generated orthophotos, which offer enhanced georeferencing accuracy, resulted in only marginal reductions in positional discrepancies. Specifically, the recalculated positional deviations were 1.161 ± 0.324 m for intersection L and 0.808 ± 0.480 m for intersection P. The corresponding speed differences were -0.397 ± 0.947 km/h and -0.616 ± 2.794 km/h, respectively. Given the superior track stabilization performance (see Fig. 7) and orthophoto matching accuracy (see Table 4), we propose that the elevated discrepancies are unlikely to stem from errors in the original orthophoto. Instead, a closer examination of the urban environments surrounding intersections L and P suggests that signal multipath effects and occlusions could be contributing factors. The presence of tall buildings around these intersections (see Fig. 18) is characteristic of densely built urban areas like Songdo and is well-documented to cause the “urban canyon effect”, where GNSS accuracy is compromised due to signal reflections and obstructions from surrounding structures [121, 122].

5. Conclusion

In this study, we have introduced a comprehensive framework for extracting georeferenced vehicle trajectories from high-altitude drone imagery, significantly advancing the capabilities of urban traffic monitoring systems. By leveraging state-of-the-art computer vision tools, deep learning models, and advanced georeferencing techniques, our end-to-end pipeline effectively addresses the challenges of vehicle detection, tracking, trajectory stabilization, and state estimation in complex urban environments. Our approach has demonstrated impressive detection performance, despite the inherent difficulties posed by high-altitude BEV perspectives. The innovative application of track stabilization after object tracking and the use of detected vehicle bounding boxes as exclusion masks during image registration have allowed us to circumvent traditional video stabilization constraints, resulting in reliable vehicle movement and state estimations. Additionally, the precise integration of GCPs within the orthophoto has enhanced georeferencing accuracy, which is crucial for detailed traffic dynamics analysis, including speed and vehicle dimension estimations.

The application of our methodology in a multi-drone experiment over 20 intersections in the Songdo International Business District has yielded two high-quality datasets: the Songdo Traffic dataset, comprising nearly 1 million unique vehicle trajectories, and the Songdo Vision dataset, consisting of over 5,000 human-annotated frames for object detection. Importantly, the Songdo Vision dataset addresses a significant gap in existing datasets by providing detailed annotations for smaller vehicles, such as motorcycles, in elevated BEV perspectives, thus enabling the development of more accurate and comprehensive AI models for urban traffic analysis. By publicly releasing these datasets along with the extraction pipeline source code, we set new benchmarks for data quality, reproducibility, and scalability in traffic research, fostering collaboration and accelerating innovation within the research community and beyond. The effectiveness of our approach is underscored by the detailed traffic dynamics analysis enabled by our datasets. The effectiveness of our approach is underscored by the detailed traffic dynamics analysis enabled by our datasets. The integration of detailed road and lane segmentations and vehicle dimension estimates facilitates a nuanced understanding of urban mobility patterns, essential for optimizing traffic flow and enhancing road safety. Moreover, comparisons between our drone-derived data and

³<https://www.agisoft.com/>

high-precision sensor data from an instrumented probe vehicle highlight the accuracy and consistency of our extraction methods in dense urban settings.

While our study makes significant contributions, we acknowledge certain limitations, such as the exclusion of smaller and non-motorized road users from the primary dataset and the manual efforts required for video and road segmentations. Future work will focus on expanding detection capabilities to include these road users and improving the efficiency of our segmentation techniques to support broader applications. Overall, our methodologies and datasets not only enhance the accuracy and scalability of traffic monitoring systems but also provide a valuable foundation for future innovations in intelligent transportation systems. By integrating drone technology with advanced computer vision and deep learning tools, we pave the way for precise and cost-effective urban traffic monitoring, with significant implications for urban planning, autonomous vehicle development, and the enhancement of smart cities.

Acknowledgments

This work was supported by research grants from the Swiss National Science Foundation under NCCR Automation (No. 51NF40_180545, N.G. and R.F.), Innosuisse (No. 101.645 IP-ENG, N.G. and R.F.), the National Research Foundation of Korea (NRF) grant funded by the Korean government (MSIT) (No. 2022R1A2C1012380, H.Y. and H.C.), and the Open Research Data (ORD) Program of the ETH Board (R.F.). The authors express their gratitude to Sohyeong Kim, Yura Tak, and Weijiang Xiong for their invaluable assistance in the data-wrangling process, Artem Vasilev for his dedicated efforts in data annotation, Jasso Espadaler Clapés for his insightful contributions to vehicle dimension estimation, and Muhammad Ahmed for his support in creating the experimental orthophoto for validation purposes. We also thank DroMii company for producing the primary orthophoto and Stanford University for providing the on-board recorded trajectories of their autonomous vehicle.

Data availability

The Songdo Traffic and Songdo Vision datasets will be available for download from [28] and [29], respectively, and accessible via <https://open-traffic.epfl.ch>. The complete source code for the trajectory extraction framework, along with the stabilization library and the associated optimization tool, will be archived in [30], [31], and [32], respectively, and will be maintained on GitHub.

Appendix A. Vehicle dimension estimation steps and implementation details

For ease of notation, the sequentially ordered BBs for a vehicle with identifier “id” in video v are denoted as $(x^{\text{id}}[k], y^{\text{id}}[k], w^{\text{id}}[k], h^{\text{id}}[k])$, where k ranges from 1 to N_v^{id} . These values, un-normalized by the image dimensions w_I and h_I , are used to calculate the vehicle’s length (L^{id}) and width (W^{id}) in meters through a structured five-step process:

Step 1 - Visibility filtering: This initial step filters out BBs that are not fully visible within the frame, focusing on fully observable vehicles. We define a visibility set \mathcal{V}^{id} containing indices k of BBs satisfying:

$$x^{\text{id}}[k] - \frac{w^{\text{id}}[k]}{2} > \varepsilon, \quad x^{\text{id}}[k] + \frac{w^{\text{id}}[k]}{2} < w_I - (\varepsilon + 1), \quad y^{\text{id}}[k] - \frac{h^{\text{id}}[k]}{2} > \varepsilon, \quad y^{\text{id}}[k] + \frac{h^{\text{id}}[k]}{2} < h_I - (\varepsilon + 1), \quad (\text{A.1})$$

where $\varepsilon > 0$ is a margin to keep BBs well within the frame’s boundaries. The detection system ensures that BBs dimensions do not exceed the frame limits, with pixel coordinates ranging from 0 to $w_I - 1$ horizontally and $h_I - 1$ vertically. The margin ε helps filter out transient BBs generated as vehicles enter or exit the frame, as the detector can identify partially visible vehicles, leading to variable BB sizes due to vehicles’ gradual appearance or disappearance at the frame boundaries.

Step 2 - Initial dimensions computation: Using the remaining BBs after Step 1, we curate the set of instantaneous vehicle lengths \mathcal{L}^{id} and widths \mathcal{W}^{id} according to the following simple rule:

$$\begin{aligned} \mathcal{L}^{\text{id}} &\triangleq \left\{ L_{\text{inf}}^{\text{id}}, \dots, L_{\text{sup}}^{\text{id}} \right\} = \left\{ \max(w^{\text{id}}[k], h^{\text{id}}[k]) \mid k \in \mathcal{V}^{\text{id}} \right\}, \\ \mathcal{W}^{\text{id}} &\triangleq \left\{ W_{\text{inf}}^{\text{id}}, \dots, W_{\text{sup}}^{\text{id}} \right\} = \left\{ \min(w^{\text{id}}[k], h^{\text{id}}[k]) \mid k \in \mathcal{V}^{\text{id}} \right\}. \end{aligned} \quad (\text{A.2})$$

Step 3 - Azimuth-based filtering: We refine the sets \mathcal{L}^{id} and \mathcal{W}^{id} using the vehicle’s azimuth estimate $\theta_k^{\text{id}} \in [0, 2\pi)$, calculated asynchronously from trajectory points in the CS of the reference frame F_v^{ref} , as follows:

$$\theta_k^{\text{id}} = \text{atan2}\left(y^{\text{id}}[\delta_k^{\text{id}}] - y^{\text{id}}[\delta_{k-1}^{\text{id}}], x^{\text{id}}[\delta_k^{\text{id}}] - x^{\text{id}}[\delta_{k-1}^{\text{id}}]\right), \quad k = 1, 2, \dots, \quad (\text{A.3})$$

where $\delta_k^{\text{id}} > 0$ is a discrete-time window growing recursively:

$$\delta_k^{\text{id}} = \delta_{k-1}^{\text{id}} + \inf_{\delta \in \mathbb{N}} \left\{ \delta \left| \sqrt{\left(\Delta_x^{\text{id}}(\delta_{k-1}^{\text{id}}, \delta) \right)^2 + \left(\Delta_y^{\text{id}}(\delta_{k-1}^{\text{id}}, \delta) \right)^2} \geq r_{\text{px}}, \delta_{k-1}^{\text{id}} + \delta \leq \sup(\mathcal{V}^{\text{id}}) \right. \right\}. \quad (\text{A.4})$$

Here, $\Delta_x^{\text{id}}(\delta_{k-1}^{\text{id}}, \delta) = x^{\text{id}}[\delta_{k-1}^{\text{id}} + \delta] - x^{\text{id}}[\delta_{k-1}^{\text{id}}]$ and $\Delta_y^{\text{id}}(\delta_{k-1}^{\text{id}}, \delta) = y^{\text{id}}[\delta_{k-1}^{\text{id}} + \delta] - y^{\text{id}}[\delta_{k-1}^{\text{id}}]$ represent the distances traveled in the x and y directions, respectively, for a step δ . The initial index $\delta_0^{\text{id}} = \inf(\mathcal{V}^{\text{id}})$ corresponds to the time index of the 1st visible BB, and $r_{\text{px}} > 0$ denotes the radius in pixels regulates the frequency of azimuth computations.

To provide a physical interpretation of r_{px} , we define $r_{\text{px}} = r_{\text{m}}/\text{GSD}$, where GSD is the ground distance per pixel (meters/pixel) and $r_{\text{m}} > 0$ is the minimum distance (meters) required for azimuth computation. This ensures azimuth calculations rely on significant vehicle movements, avoiding inaccuracies during stationary periods. GSD can be calculated using camera specifications and flight altitude or derived from the orthomosaic.

If at least one azimuth is available θ_k^{id} ($k \geq 1$), we further refine \mathcal{L}^{id} and \mathcal{W}^{id} using all available θ_k^{id} as follows:

$$\begin{aligned} \mathcal{L}^{\text{id}} &= \left\{ L_i^{\text{id}} \mid L_i^{\text{id}} \in \mathcal{L}^{\text{id}}, i \in [\delta_{k-1}^{\text{id}}, \delta_k^{\text{id}}] \text{ if } |\theta_k - \phi_j| \leq \bar{\theta}, \text{ for any } \phi_j \in \Phi \right\}, \\ \mathcal{W}^{\text{id}} &= \left\{ W_i^{\text{id}} \mid W_i^{\text{id}} \in \mathcal{W}^{\text{id}}, i \in [\delta_{k-1}^{\text{id}}, \delta_k^{\text{id}}] \text{ if } |\theta_k - \phi_j| \leq \bar{\theta}, \text{ for any } \phi_j \in \Phi \right\}, \end{aligned} \quad (\text{A.5})$$

where $\Phi = \{0, \pi/2, \pi, 3\pi/2, 2\pi\}$ is a set of cardinal directions and $\bar{\theta} > 0$ is the maximum azimuth deviation allowed. The parameter $\bar{\theta}$ accounts for vehicle orientations that are non-parallel to the image axes, with a smaller $\bar{\theta}$ indicating more stringent filtering, thus ensuring only representative vehicle dimensions are considered.

When no azimuth data is available (e.g., stationary or parked vehicles), we filter BBs exhibiting square-like proportions, as these often reflect non-parallel parking or partial occlusions that compromise accuracy. This is achieved by a ratio-based criterion:

$$\mathcal{L}^{\text{id}} = \left\{ L_i^{\text{id}} \mid L_i^{\text{id}} \in \mathcal{L}^{\text{id}}, \frac{L_i^{\text{id}}}{W_i^{\text{id}}} \geq \kappa_c \right\}, \quad \mathcal{W}^{\text{id}} = \left\{ W_i^{\text{id}} \mid W_i^{\text{id}} \in \mathcal{W}^{\text{id}}, \frac{L_i^{\text{id}}}{W_i^{\text{id}}} \geq \kappa_c \right\}. \quad (\text{A.6})$$

Here, $\kappa_c > 1$ is a class-specific threshold for the degree of non-squareness, with ratios $L_i^{\text{id}}/W_i^{\text{id}}$ approaching 1 indicating square-like dimensions, which are atypical in the Songdo footage and are therefore flagged as unreliable.

Step 4 - Final dimension computation: After implementing Steps 1 to 3, if the sets \mathcal{L}^{id} and \mathcal{W}^{id} are not empty, the unique vehicle dimensions in pixels are determined as follows:

$$L_{\text{px}}^{\text{id}} = Q_{\text{lower}}(\mathcal{L}^{\text{id}}), \quad W_{\text{px}}^{\text{id}} = Q_{\text{lower}}(\mathcal{W}^{\text{id}}). \quad (\text{A.7})$$

Here, $Q_{\text{lower}}(\cdot)$ computes the first quartile, indicating the value below which 25% of observations fall. This measure is preferred due to the leniency of $\bar{\theta}$, resulting in dimensions that meet or exceed the ground truth, while mean or median methods often yield overly conservative estimates. Minimum values are avoided to prevent errors from partial occlusions.

Step 5 - Real-world conversion: In this final step, the vehicle dimensions $L_{\text{px}}^{\text{id}}$ and $W_{\text{px}}^{\text{id}}$ are converted from pixels to meters by placing a hypothetical BB at the center of the video frame. Centering the BB leverages the higher precision of the orthophoto, enhanced by strategically placed GCPs at intersection edges. The conversion uses a three-point BB decomposition defined as:

$$p_{\text{px}1}^{\text{id}} = \frac{1}{2}(w_I, h_I), \quad p_{\text{px}2}^{\text{id}} = \frac{1}{2}(w_I, h_I + W_{\text{px}}^{\text{id}}), \quad p_{\text{px}3}^{\text{id}} = \frac{1}{2}(w_I + L_{\text{px}}^{\text{id}}, h_I). \quad (\text{A.8})$$

These points are transformed to local Cartesian coordinates using $H_v^{\text{ref} \rightarrow \text{ortho}}$ and $T_i^{\text{ortho} \rightarrow \text{world}}$ (see Section 3.6) yielding real-world coordinates p_1^{id} , p_2^{id} , and p_3^{id} . Finally, the real-world vehicle dimensions L^{id} and W^{id} are determined using appropriate geometric relations:

$$L^{\text{id}} = 2\|p_3^{\text{id}} - p_1^{\text{id}}\|, \quad W^{\text{id}} = 2\|p_2^{\text{id}} - p_1^{\text{id}}\|, \quad (\text{A.9})$$

where $\|\cdot\|$ is the Euclidean norm of a vector, effectively measuring the physical distances between the points.

All steps outlined above should employ the unstabilized BBs from \mathcal{T}_v , with the sole exception of the azimuth angle calculation, θ_k^{id} , which should be based on the stabilized vehicle trajectories contained in $\mathcal{T}_v^{\text{ref}}$.

Implementation details

In our experiment, we set $\varepsilon = 4$, $\bar{\theta} = 15^\circ$, $r_{\text{m}} = 1.25$, and derived GSD = 0.02725 based on camera specifications and an average altitude of 145 m, resulting in $r_{\text{px}} \approx 45.87$. The calibration of r_{m} is essential for effective azimuth-based

filtering and is primarily influenced by the quality of the track stabilization process. r_m must be sufficiently large to avoid triggering new azimuth computations from drone movement artifacts while remaining small enough to capture azimuth updates during brief intervals of vehicle alignment with the image axes, particularly during road turns. This calibration is essential for vehicles on roads misaligned with the image axes due to infrastructure layout or drone orientation. Accurate dimension estimation can be achieved if, during brief moments of alignment, an azimuth satisfying $\bar{\theta}$ is computed.

The class-dependent threshold parameters κ_c , used in (A.6) to filter dimensions of stationary vehicles, were derived by applying Q_{lower} to the empirical distributions of class-filtered L/W ratios from moving vehicles. Extensive trajectory data analysis yielded specific thresholds for each vehicle category: $\kappa_{\text{car}} = 1.83$, $\kappa_{\text{bus}} = 2.85$, $\kappa_{\text{truck}} = 1.7$, and $\kappa_{\text{motorcycle}} = 1.8$. To obtain reliable estimates of L and W , we enforced stricter azimuth angle constraints ($\bar{\theta} = 5^\circ$) and set κ_c to ∞ to retain BBs only from vehicles perfectly aligned with the reference frame F_v^{ref} .

Appendix B. Vehicle kinematics computation and tuning

The raw speed of a vehicle with identifier id at time k is computed as the Euclidean distance between two consecutive interpolated trajectory points $(x_L^{\text{id}}[k], y_L^{\text{id}}[k])$ and $(x_L^{\text{id}}[k-1], y_L^{\text{id}}[k-1])$ in the local coordinate system, divided by the time step $\Delta t = t_k - t_{k-1}$, which is equal to FPS^{-1} for the processed video v .

To smooth the speed data $v^{\text{id}}[k]$, we apply a Gaussian filter through a discrete convolution with a 1D Gaussian kernel:

$$\tilde{v}^{\text{id}}[k] = \sum_{i=-M}^M v^{\text{id}}[r(k+i)] \cdot g_\sigma[i], \quad k \in \{2, \dots, N_v^{\text{id}}\}, \quad (\text{B.1})$$

where $g_\sigma[i] = \frac{1}{\sqrt{2\pi}\sigma} \exp\left(-\frac{i^2}{2\sigma^2}\right)$, $\sigma > 0$ is the standard deviation, and M is set as 3σ to encompass the significant range of the Gaussian function $g_\sigma[i]$. The reflect function $r(j)$ handles boundary conditions by mirroring the data at the edges:

$$r(j) = j + 2(N_v^{\text{id}} - j) \cdot \mathbf{1}(j > N_v^{\text{id}}) - 2(j-1) \cdot \mathbf{1}(j < 1), \quad (\text{B.2})$$

where the indicator function $\mathbf{1}(\cdot)$ effectively reflects indices when j lies outside the range $[1, N_v^{\text{id}}]$.

The acceleration profile $a^{\text{id}}[k]$ is computed by taking the backward difference of consecutive smoothed speed values: $a^{\text{id}}[k] = (\tilde{v}^{\text{id}}[k] - \tilde{v}^{\text{id}}[k-1])/\Delta t$, for $k \in 3, \dots, N_v^{\text{id}}$. Only indices that satisfy $k \in \mathcal{V}^{\text{id}}$ retain $\tilde{v}^{\text{id}}[k]$ and $a^{\text{id}}[k]$ in the dataset, where \mathcal{V}^{id} is the visibility set defined in (A.1). This ensures that kinematic computations are unaffected by changes in BBs as vehicles enter or exit the camera's FoV.

The standard deviation σ of the Gaussian kernel is the sole tuning parameter for smoothing speed data. We use the AV data to determine the optimal value of σ by assessing the relationship between various σ values and corresponding speed estimation errors (11) from the AV's on-board RTK-GNSS across multiple intersections. The evaluation reveals that the mean optimal σ across all intersections is 13.78, while the weighted average, considering the lengths of observed AV trajectories, is 13.81. We, therefore, set σ at 14 frames, corresponding to 0.467 seconds at a frame rate of 29.97 FPS, to achieve an optimal balance between smoothing and detail retention across varied scenarios. Notably, we also experimented with the Savitzky-Golay filter [123], which yielded comparable results to our Gaussian filter approach.

References

- [1] R. Zhang, S. Newman, M. Ortolani, S. Silvestri, A network tomography approach for traffic monitoring in smart cities, *IEEE Transactions on Intelligent Transportation Systems* 19 (2018) 2268–2278. doi:[10.1109/TITS.2018.2829086](https://doi.org/10.1109/TITS.2018.2829086).
- [2] S. Sivaraman, M. M. Trivedi, Looking at vehicles on the road: A survey of vision-based vehicle detection, tracking, and behavior analysis, *IEEE Transactions on Intelligent Transportation Systems* 14 (2013) 1773–1795. doi:[10.1109/TITS.2013.2266661](https://doi.org/10.1109/TITS.2013.2266661).
- [3] Z. Yang, L. S. Pun-Cheng, Vehicle detection in intelligent transportation systems and its applications under varying environments: A review, *Image and Vision Computing* 69 (2018) 143–154. doi:[10.1016/j.imavis.2017.09.008](https://doi.org/10.1016/j.imavis.2017.09.008).
- [4] H. Ghahremannezhad, H. Shi, C. Liu, Object detection in traffic videos: A survey, *IEEE Transactions on Intelligent Transportation Systems* (2023). doi:[10.1109/TITS.2023.3258683](https://doi.org/10.1109/TITS.2023.3258683).

[5] B. Li, 3D fully convolutional network for vehicle detection in point cloud, in: 2017 IEEE/RSJ International Conference on Intelligent Robots and Systems (IROS), IEEE, 2017, pp. 1513–1518. doi:[10.1109/IROS.2017.8205955](https://doi.org/10.1109/IROS.2017.8205955).

[6] Z. Zhang, J. Zheng, H. Xu, X. Wang, Vehicle detection and tracking in complex traffic circumstances with roadside LiDAR, *Transportation Research Record* 2673 (2019) 62–71. doi:[10.1177/03611981198444](https://doi.org/10.1177/03611981198444).

[7] E. Sifuentes, O. Casas, R. Pallas-Areny, Wireless magnetic sensor node for vehicle detection with optical wake-up, *IEEE Sensors journal* 11 (2011) 1669–1676. doi:[10.1109/JSEN.2010.2103937](https://doi.org/10.1109/JSEN.2010.2103937).

[8] Q. Wang, J. Zheng, H. Xu, B. Xu, R. Chen, Roadside magnetic sensor system for vehicle detection in urban environments, *IEEE Transactions on Intelligent Transportation Systems* 19 (2017) 1365–1374. doi:[10.1109/TITS.2017.2723908](https://doi.org/10.1109/TITS.2017.2723908).

[9] J. Fang, H. Meng, H. Zhang, X. Wang, A low-cost vehicle detection and classification system based on unmodulated continuous-wave radar, in: 2007 IEEE Intelligent Transportation Systems Conference, IEEE, 2007, pp. 715–720. doi:[10.1109/ITSC.2007.4357739](https://doi.org/10.1109/ITSC.2007.4357739).

[10] S. J. Park, T. Y. Kim, S. M. Kang, K. H. Koo, A novel signal processing technique for vehicle detection radar, in: IEEE MTT-S International Microwave Symposium Digest, 2003, volume 1, IEEE, 2003, pp. 607–610. doi:[10.1109/MWSYM.2003.1211012](https://doi.org/10.1109/MWSYM.2003.1211012).

[11] T. Seo, A. M. Bayen, T. Kusakabe, Y. Asakura, Traffic state estimation on highway: A comprehensive survey, *Annual Reviews in Control* 43 (2017) 128–151. doi:[10.1016/j.arcontrol.2017.03.005](https://doi.org/10.1016/j.arcontrol.2017.03.005).

[12] A. Kouvelas, M. Saeedmanesh, N. Geroliminis, A linear-parameter-varying formulation for model predictive perimeter control in multi-region mfd urban networks, *Transportation Science* 57 (2023) 1496–1515. doi:[10.1287/trsc.2022.0103](https://doi.org/10.1287/trsc.2022.0103).

[13] D. Tsitsokas, A. Kouvelas, N. Geroliminis, Two-layer adaptive signal control framework for large-scale dynamically-congested networks: Combining efficient max pressure with perimeter control, *Transportation Research Part C: Emerging Technologies* 152 (2023) 104128. doi:[10.1016/j.trc.2023.104128](https://doi.org/10.1016/j.trc.2023.104128).

[14] M. Hassanalian, A. Abdelkefi, Classifications, applications, and design challenges of drones: A review, *Progress in Aerospace Sciences* 91 (2017) 99–131. doi:[10.1016/j.paerosci.2017.04.003](https://doi.org/10.1016/j.paerosci.2017.04.003).

[15] M. A. Khan, W. Ectors, T. Bellemans, D. Janssens, G. Wets, Unmanned aerial vehicle-based traffic analysis: Methodological framework for automated multivehicle trajectory extraction, *Transportation Research Record* 2626 (2017) 25–33. doi:[10.3141/2626-04](https://doi.org/10.3141/2626-04).

[16] F. Outay, H. A. Mengash, M. Adnan, Applications of unmanned aerial vehicle (UAV) in road safety, traffic and highway infrastructure management: Recent advances and challenges, *Transportation research part A: policy and practice* 141 (2020) 116–129. doi:[10.1016/j.tra.2020.09.018](https://doi.org/10.1016/j.tra.2020.09.018).

[17] J. Espadaler-Clapés, R. Fonod, E. Barmpounakis, N. Geroliminis, Continuous monitoring of a signalized intersection using unmanned aerial vehicles, in: 2023 IEEE 26th International Conference on Intelligent Transportation Systems (ITSC), IEEE, 2023, pp. 5338–5343. doi:[10.1109/ITSC57777.2023.10422673](https://doi.org/10.1109/ITSC57777.2023.10422673).

[18] A. Gohari, A. Ahmad, R. A. Rahim, A. S. M. Supa’at, S. A. Razak, M. Gismalla, Involvement of surveillance drones in smart cities: a systematic review, *IEEE Access* 10 (2022) 56611–56628. doi:[10.1109/access.2022.3177904](https://doi.org/10.1109/access.2022.3177904).

[19] D. Kim, Pedestrian and bicycle volume data collection using drone technology, *Journal of Urban Technology* 27 (2020) 45 – 60. doi:[10.1080/10630732.2020.1715158](https://doi.org/10.1080/10630732.2020.1715158).

[20] V. Mahajan, E. Barmpounakis, M. R. Alam, N. Geroliminis, C. Antoniou, Treating noise and anomalies in vehicle trajectories from an experiment with a swarm of drones, *IEEE Transactions on Intelligent Transportation Systems* 24 (2023) 9055–9067. doi:[10.1109/TITS.2023.3268712](https://doi.org/10.1109/TITS.2023.3268712).

[21] M. Paipuri, E. Barmpounakis, N. Geroliminis, L. Leclercq, Empirical observations of multi-modal network-level models: Insights from the pNEUMA experiment, *Transportation Research Part C: Emerging Technologies* 131 (2021) 103300. doi:[10.1016/j.trc.2021.103300](https://doi.org/10.1016/j.trc.2021.103300).

[22] S. Kim, Y. Tak, E. Barmpounakis, N. Geroliminis, Monitoring Outdoor Parking in Urban Areas With Unmanned Aerial Vehicles, *IEEE Transactions on Intelligent Transportation Systems* (2024). doi:[10.1109/TITS.2024.3397588](https://doi.org/10.1109/TITS.2024.3397588).

[23] E. Barmpounakis, M. Montesinos-Ferrer, E. J. Gonzales, N. Geroliminis, Empirical investigation of the emission-macroscopic fundamental diagram, *Transportation Research Part D: Transport and Environment* 101 (2021) 103090. doi:[10.1016/j.trd.2021.103090](https://doi.org/10.1016/j.trd.2021.103090).

[24] J. Espadaler-Clapés, E. Barmpounakis, N. Geroliminis, Traffic congestion and noise emissions with detailed vehicle trajectories from UAVs, *Transportation Research Part D: Transport and Environment* 121 (2023) 103822. doi:[10.1016/j.trd.2023.103822](https://doi.org/10.1016/j.trd.2023.103822).

[25] L. Jian, Z. Li, X. Yang, W. Wu, A. Ahmad, G. Jeon, Combining unmanned aerial vehicles with artificial-intelligence technology for traffic-congestion recognition: electronic eyes in the skies to spot clogged roads, *IEEE Consumer Electronics Magazine* 8 (2019) 81–86. doi:[10.1109/MCE.2019.2892286](https://doi.org/10.1109/MCE.2019.2892286).

[26] N. A. Khan, N. Jhanjhi, S. N. Brohi, R. S. A. Usmani, A. Nayyar, Smart traffic monitoring system using unmanned aerial vehicles (UAVs), *Computer Communications* 157 (2020) 434–443. doi:[10.1016/j.comcom.2020.04.049](https://doi.org/10.1016/j.comcom.2020.04.049).

[27] E. Barmpounakis, N. Geroliminis, On the new era of urban traffic monitoring with massive drone data: The pNEUMA large-scale field experiment, *Transportation research part C: emerging technologies* 111 (2020) 50–71. doi:[10.1016/j.trc.2019.11.023](https://doi.org/10.1016/j.trc.2019.11.023).

[28] R. Fonod, H. Cho, H. Yeo, N. Geroliminis, Songdo Traffic: High Accuracy Georeferenced Vehicle Trajectories from a Large-Scale Study in a Smart City, 2024. doi:[10.5281/zenodo.13828384](https://doi.org/10.5281/zenodo.13828384).

[29] R. Fonod, H. Cho, H. Yeo, N. Geroliminis, Songdo Vision: Vehicle Annotations from High-Altitude BeV Drone Imagery in a Smart City, 2024. doi:[10.5281/zenodo.13828408](https://doi.org/10.5281/zenodo.13828408).

[30] R. Fonod, H. Cho, Geo-trax: A Comprehensive Framework for Georeferenced Vehicle Trajectory Extraction from Drone Imagery, 2024. URL: <https://github.com/rfonod/geo-trax>. doi:[10.5281/zenodo.12119542](https://doi.org/10.5281/zenodo.12119542).

[31] R. Fonod, Stabilo: A Comprehensive Python Library for Video and Trajectory Stabilization with User-Defined Masks, 2024. URL: <https://github.com/rfonod/stabilo>. doi:[10.5281/zenodo.12117092](https://doi.org/10.5281/zenodo.12117092).

[32] R. Fonod, Stabilo Optimize: A Framework for Comprehensive Evaluation and Analysis for the Stabilo Library, 2024. URL: <https://github.com/rfonod/stabilo-optimize>. doi:[10.5281/zenodo.13828430](https://doi.org/10.5281/zenodo.13828430), (The source code will be made available at the time of publication).

[33] N. A. Mandellos, I. Keramitsoglou, C. T. Kiranoudis, A background subtraction algorithm for detecting and tracking vehicles, *Expert Systems with Applications* 38 (2011) 1619–1631. doi:[10.1016/j.eswa.2010.07.083](https://doi.org/10.1016/j.eswa.2010.07.083).

[34] L. Gokul, P. Adarsh, G. Vinayan, G. Gokuldath, M. Ponnalar, S. Aswini, Lucas Kanade based Optical Flow for Vehicle Motion Tracking and Velocity Estimation, in: 2023 International Conference on Control, Communication and Computing (ICCC), IEEE, 2023, pp. 1–6. doi:[10.1109/ICCC57789.2023.10165227](https://doi.org/10.1109/ICCC57789.2023.10165227).

[35] J.-H. Choi, K.-H. Lee, K.-C. Cha, J.-S. Kwon, D.-W. Kim, H.-K. Song, Vehicle tracking using template matching based on feature points, in: 2006 IEEE International Conference on Information Reuse & Integration, IEEE, 2006, pp. 573–577. doi:[10.1109/IRI.2006.252477](https://doi.org/10.1109/IRI.2006.252477).

[36] B. Coifman, D. Beymer, P. McLauchlan, J. Malik, A real-time computer vision system for vehicle tracking and traffic surveillance, *Transportation Research Part C: Emerging Technologies* 6 (1998) 271–288. doi:[10.1016/S0968-090X\(98\)00019-9](https://doi.org/10.1016/S0968-090X(98)00019-9).

[37] X. Cao, C. Wu, J. Lan, P. Yan, X. Li, Vehicle detection and motion analysis in low-altitude airborne video under urban environment, *IEEE Transactions on Circuits and Systems for Video Technology* 21 (2011) 1522–1533. doi:[10.1109/TCSVT.2011.2162274](https://doi.org/10.1109/TCSVT.2011.2162274).

[38] B.-F. Wu, C.-C. Kao, C.-L. Jen, Y.-F. Li, Y.-H. Chen, J.-H. Juang, A relative-discriminative-histogram-of-oriented-gradients-based particle filter approach to vehicle occlusion handling and tracking, *IEEE Transactions on Industrial Electronics* 61 (2013) 4228–4237. doi:[10.1109/TIE.2013.2284131](https://doi.org/10.1109/TIE.2013.2284131).

[39] M. A. Khan, W. Ectors, T. Bellemans, Y. Ruichek, D. Janssens, G. Wets, et al., Unmanned aerial vehicle-based traffic analysis: A case study to analyze traffic streams at urban roundabouts, *Procedia computer science* 130 (2018) 636–643. doi:[10.1016/j.procs.2018.04.114](https://doi.org/10.1016/j.procs.2018.04.114).

[40] W. Kim, C. Jung, Illumination-invariant background subtraction: Comparative review, models, and prospects, *IEEE Access* 5 (2017) 8369–8384. doi:[10.1109/ACCESS.2017.2699227](https://doi.org/10.1109/ACCESS.2017.2699227).

[41] T. Zhang, P. J. Jin, A longitudinal scanline based vehicle trajectory reconstruction method for high-angle traffic video, *Transportation Research Part C: Emerging Technologies* 103 (2019) 104–128. doi:[10.1016/j.trc.2019.03.015](https://doi.org/10.1016/j.trc.2019.03.015).

[42] W. Liu, D. Anguelov, D. Erhan, C. Szegedy, S. Reed, C.-Y. Fu, A. C. Berg, SSD: Single Shot Multibox Detector, in: *Computer Vision – ECCV 2016*, Springer, 2016, pp. 21–37. doi:[10.1007/978-3-319-46448-0_2](https://doi.org/10.1007/978-3-319-46448-0_2).

[43] R. Girshick, J. Donahue, T. Darrell, J. Malik, Rich feature hierarchies for accurate object detection and semantic segmentation, in: *Proceedings of the IEEE conference on computer vision and pattern recognition*, 2014, pp. 580–587. doi:[10.1109/CVPR.2014.81](https://doi.org/10.1109/CVPR.2014.81).

[44] J. Redmon, S. Divvala, R. Girshick, A. Farhadi, You Only Look Once: Unified, Real-Time Object Detection, in: *Proceedings of the IEEE conference on computer vision and pattern recognition*, 2016, pp. 779–788. doi:[10.1109/CVPR.2016.91](https://doi.org/10.1109/CVPR.2016.91).

[45] S. Ren, K. He, R. Girshick, J. Sun, Faster R-CNN: Towards Real-Time Object Detection with Region Proposal Networks, *IEEE Transactions on Pattern Analysis and Machine Intelligence* 39 (2017) 1137–1149. doi:[10.1109/TPAMI.2016.2577031](https://doi.org/10.1109/TPAMI.2016.2577031).

[46] S.-C. Hsu, C.-L. Huang, C.-H. Chuang, Vehicle detection using simplified fast R-CNN, in: *2018 International Workshop on Advanced Image Technology (IWAIT)*, IEEE, 2018, pp. 1–3. doi:[10.1109/IWAIT.2018.8369767](https://doi.org/10.1109/IWAIT.2018.8369767).

[47] W. Zhan, L. Sun, D. Wang, H. Shi, A. Clausse, M. Naumann, J. Kummerle, H. Konigshof, C. Stiller, A. de La Fortelle, et al., Interaction dataset: An international, adversarial and cooperative motion dataset in interactive driving scenarios with semantic maps, *arXiv:1910.03088 [cs, eess]* (2019). doi:[10.48550/arXiv.1910.03088](https://doi.org/10.48550/arXiv.1910.03088).

[48] J. Redmon, A. Farhadi, YOLOv3: An Incremental Improvement, *arXiv preprint arXiv:1804.02767* (2018). doi:[10.48550/arXiv.1804.02767](https://doi.org/10.48550/arXiv.1804.02767). [arXiv:1804.02767](https://arxiv.org/abs/1804.02767).

[49] A. Bochkovskiy, C.-Y. Wang, H.-Y. M. Liao, YOLOv4: Optimal Speed and Accuracy of Object Detection, *arXiv preprint arXiv:2004.10934* (2020). doi:[10.48550/arXiv.2004.10934](https://doi.org/10.48550/arXiv.2004.10934).

[50] G. Jocher, YOLOv5 by Ultralytics, 2020. URL: <https://github.com/ultralytics/yolov5>. doi:[10.5281/zenodo.7347926](https://doi.org/10.5281/zenodo.7347926).

[51] C. Li, L. Li, H. Jiang, K. Weng, Y. Geng, L. Li, Z. Ke, Q. Li, M. Cheng, W. Nie, Y. Li, B. Zhang, Y. Liang, L. Zhou, X. Xu, X. Chu, X. Wei, X. Wei, YOLOv6: A Single-Stage Object Detection Framework for Industrial Applications, *arXiv* (2022). doi:[10.48550/arXiv.2209.02976v1](https://doi.org/10.48550/arXiv.2209.02976v1).

[52] C.-Y. Wang, A. Bochkovskiy, H.-Y. M. Liao, YOLOv7: Trainable Bag-of-Freebies Sets New State-of-the-Art for Real-Time Object Detectors, in: *Proceedings of the IEEE/CVF Conference on Computer Vision and Pattern Recognition*, 2023, pp. 7464–7475. doi:[10.1109/CVPR52729.2023.00721](https://doi.org/10.1109/CVPR52729.2023.00721).

[53] G. Jocher, A. Chaurasia, J. Qiu, Ultralytics YOLO, 2023. URL: <https://github.com/ultralytics/ultralytics>. doi:[10.5281/zenodo.13942966](https://doi.org/10.5281/zenodo.13942966).

[54] C.-Y. Wang, I.-H. Yeh, H.-Y. M. Liao, YOLOv9: Learning What You Want to Learn Using Programmable Gradient Information, arXiv (2024). doi:[arXiv:2402.13616](https://arxiv.org/abs/2402.13616).

[55] A. Wang, H. Chen, L. Liu, K. Chen, Z. Lin, J. Han, G. Ding, YOLOv10: Real-Time End-to-End Object Detection, arXiv (2024). doi:[arXiv:2405.14458](https://arxiv.org/abs/2405.14458).

[56] Q.-C. Mao, H.-M. Sun, L.-Q. Zuo, R.-S. Jia, Finding every car: a traffic surveillance multi-scale vehicle object detection method, *Applied Intelligence* 50 (2020) 3125–3136. doi:[10.1007/s10489-020-01704-5](https://doi.org/10.1007/s10489-020-01704-5).

[57] Y. Zhang, Z. Guo, J. Wu, Y. Tian, H. Tang, X. Guo, Real-Time Vehicle Detection Based on Improved YOLO v5, *Sustainability* 14 (2022) 12274. doi:[10.3390/su141912274](https://doi.org/10.3390/su141912274).

[58] N. Carion, F. Massa, G. Synnaeve, N. Usunier, A. Kirillov, S. Zagoruyko, End-to-end object detection with transformers, in: *Computer Vision – ECCV 2020*, Springer, 2020, pp. 213–229. doi:[10.1007/978-3-030-58452-8_13](https://doi.org/10.1007/978-3-030-58452-8_13).

[59] X. Zhu, W. Su, L. Lu, B. Li, X. Wang, J. Dai, Deformable DETR: Deformable Transformers for End-to-End Object Detection, arXiv (2021). doi:[arXiv:2010.04159v4](https://arxiv.org/abs/2010.04159v4).

[60] Z. Liu, Y. Lin, Y. Cao, H. Hu, Y. Wei, Z. Zhang, S. Lin, B. Guo, Swin transformer: Hierarchical vision transformer using shifted windows, in: *2021 IEEE/CVF International Conference on Computer Vision (ICCV)*, IEEE Computer Society, Los Alamitos, CA, USA, 2021, pp. 9992–10002. doi:[10.1109/ICCV48922.2021.00986](https://doi.org/10.1109/ICCV48922.2021.00986).

[61] Y. Zhao, W. Lv, S. Xu, J. Wei, G. Wang, Q. Dang, Y. Liu, J. Chen, DETRs Beat YOLOs on Real-time Object Detection, in: *2024 IEEE/CVF Conference on Computer Vision and Pattern Recognition (CVPR)*, IEEE Computer Society, Los Alamitos, CA, USA, 2024, pp. 16965–16974. doi:[10.1109/CVPR52733.2024.01605](https://doi.org/10.1109/CVPR52733.2024.01605).

[62] J. He, H. Chen, B. Liu, S. Luo, J. Liu, Enhancing YOLO for occluded vehicle detection with grouped orthogonal attention and dense object repulsion, *Scientific Reports* 14 (2024) 19650. doi:[10.1038/s41598-024-70695-x](https://doi.org/10.1038/s41598-024-70695-x).

[63] G. Adaimi, S. Kreiss, A. Alahi, Traffic perception from aerial images using butterfly fields, *Transportation Research Part C: Emerging Technologies* 153 (2023) 104181. doi:[10.1016/j.trc.2023.104181](https://doi.org/10.1016/j.trc.2023.104181).

[64] J. Wu, Q. Man, X. Yang, P. Dong, X. Ma, C. Liu, C. Han, Fine Classification of Urban Tree Species Based on UAV-Based RGB Imagery and LiDAR Data, *Forests* 15 (2024) 390. doi:[10.3390/f15020390](https://doi.org/10.3390/f15020390).

[65] Q. Ha, K. Watanabe, T. Karasawa, Y. Ushiku, T. Harada, MFNet: Towards real-time semantic segmentation for autonomous vehicles with multi-spectral scenes, in: *2017 IEEE/RSJ International Conference on Intelligent Robots and Systems (IROS)*, IEEE, 2017, pp. 5108–5115. doi:[10.1109/IROS.2017.8206396](https://doi.org/10.1109/IROS.2017.8206396).

[66] A. Yilmaz, O. Javed, M. Shah, Object tracking: A survey, *ACM Comput. Surv.* 38 (2006) 13–es. doi:[10.1145/1177352.117735](https://doi.org/10.1145/1177352.117735).

[67] R. E. Kalman, A New Approach to Linear Filtering and Prediction Problems, *Journal of Basic Engineering* 82 (1960) 35–45. doi:[10.1115/1.3662552](https://doi.org/10.1115/1.3662552).

[68] H. W. Kuhn, The Hungarian Method for the Assignment Problem, *Naval Research Logistics Quarterly* 2 (1955) 83–97. doi:[10.1002/nav.3800020109](https://doi.org/10.1002/nav.3800020109).

[69] J.-W. Hsieh, S.-H. Yu, Y.-S. Chen, W.-F. Hu, Automatic traffic surveillance system for vehicle tracking and classification, *IEEE Transactions on Intelligent Transportation Systems* 7 (2006) 175–187. doi:[10.1109/TITS.2006.874722](https://doi.org/10.1109/TITS.2006.874722).

[70] Z. Kim, M. Cao, Evaluation of feature-based vehicle trajectory extraction algorithms, in: *13th International IEEE Conference on Intelligent Transportation Systems*, IEEE, 2010, pp. 99–104. doi:[10.1109/ITSC.2010.5625278](https://doi.org/10.1109/ITSC.2010.5625278).

[71] A. Y. Chen, Y.-L. Chiu, M.-H. Hsieh, P.-W. Lin, O. Angah, Conflict analytics through the vehicle safety space in mixed traffic flows using UAV image sequences, *Transportation Research Part C: Emerging Technologies* 119 (2020) 102744. doi:[10.1016/j.trc.2020.102744](https://doi.org/10.1016/j.trc.2020.102744).

[72] A. Bewley, Z. Ge, L. Ott, F. Ramos, B. Upcroft, Simple online and realtime tracking, in: *2016 IEEE international conference on image processing (ICIP)*, IEEE, 2016, pp. 3464–3468. doi:[10.1109/ICIP.2016.7533003](https://doi.org/10.1109/ICIP.2016.7533003).

[73] J. Cao, J. Pang, X. Weng, R. Khirodkar, K. Kitani, Observation-Centric SORT: Rethinking SORT for Robust Multi-Object Tracking, in: Proceedings of the IEEE/CVF conference on computer vision and pattern recognition, 2023, pp. 9686–9696. doi:[10.1109/CVPR52729.2023.00934](https://doi.org/10.1109/CVPR52729.2023.00934).

[74] Y. Zhang, P. Sun, Y. Jiang, D. Yu, F. Weng, Z. Yuan, P. Luo, W. Liu, X. Wang, Bytetrack: Multi-object tracking by associating every detection box, in: European Conference on Computer Vision, Springer, 2022, pp. 1–21. doi:[10.1007/978-3-031-20047-2_1](https://doi.org/10.1007/978-3-031-20047-2_1).

[75] N. Aharon, R. Orfaig, B.-Z. Bobrovsky, BoT-SORT: Robust associations multi-pedestrian tracking, ArXiv (2022). doi:[arXiv:2206.14651v2](https://arxiv.org/abs/2206.14651v2).

[76] N. Wojke, A. Bewley, D. Paulus, Simple online and realtime tracking with a deep association metric, in: 2017 IEEE international conference on image processing (ICIP), IEEE, 2017, pp. 3645–3649. doi:[10.1109/ICIP.2017.8296962](https://doi.org/10.1109/ICIP.2017.8296962).

[77] Y. Du, Z. Zhao, Y. Song, Y. Zhao, F. Su, T. Gong, H. Meng, StrongSORT: Make DeepSORT Great Again, IEEE Transactions on Multimedia (2023). doi:[10.1109/TMM.2023.3240881](https://doi.org/10.1109/TMM.2023.3240881).

[78] Y. Zhang, C. Wang, X. Wang, W. Zeng, W. Liu, FairMOT: On the Fairness of Detection and Re-identification in Multiple Object Tracking, International Journal of Computer Vision 129 (2021) 3069–3087. doi:[10.1007/s11263-021-01513-4](https://doi.org/10.1007/s11263-021-01513-4).

[79] A. Milan, L. Leal-Taixé, I. Reid, S. Roth, K. Schindler, MOT16: A benchmark for multi-object tracking, arXiv (2016). doi:[10.48550/arXiv.1603.00831](https://arxiv.org/abs/1603.00831).

[80] P. Dendorfer, H. Rezatofighi, A. Milan, J. Shi, D. Cremers, I. Reid, S. Roth, K. Schindler, L. Leal-Taixé, MOT20: A benchmark for multi object tracking in crowded scenes, arXiv (2020). doi:[10.48550/arXiv.2003.09003](https://arxiv.org/abs/2003.09003).

[81] P. Dendorfer, A. Osep, A. Milan, K. Schindler, D. Cremers, I. Reid, S. Roth, L. Leal-Taixé, MOTChallenge: A Benchmark for Single-Camera Multiple Target Tracking, International Journal of Computer Vision 129 (2021) 845–881. doi:[10.1007/s11263-020-01393-0](https://doi.org/10.1007/s11263-020-01393-0).

[82] E. Mingkhwan, W. Khawsuk, Digital image stabilization technique for fixed camera on small size drone, in: 2017 Third Asian Conference on Defence Technology (ACDT), IEEE, 2017, pp. 12–19. doi:[10.1109/ACDT.2017.7886149](https://doi.org/10.1109/ACDT.2017.7886149).

[83] E. N. Barmpounakis, E. I. Vlahogianni, J. C. Golias, A. Babinec, How accurate are small drones for measuring microscopic traffic parameters?, Transportation letters 11 (2019) 332–340. doi:[10.1080/19427867.2017.1354433](https://doi.org/10.1080/19427867.2017.1354433).

[84] R. Kumar, H. S. Sawhney, J. C. Asmuth, A. Pope, S. Hsu, Registration of video to geo-referenced imagery, in: Proceedings of the 14th International Conference on Pattern Recognition, volume 2, IEEE, 1998, pp. 1393–1400. doi:[10.1109/ICPR.1998.711963](https://doi.org/10.1109/ICPR.1998.711963).

[85] D. G. Lowe, Distinctive Image Features from Scale-Invariant Keypoints, International journal of computer vision 60 (2004) 91–110. doi:[10.1023/B:VISI.0000029664.99615.94](https://doi.org/10.1023/B:VISI.0000029664.99615.94).

[86] R. Arandjelović, A. Zisserman, Three things everyone should know to improve object retrieval, in: 2012 IEEE Conference on Computer Vision and Pattern Recognition, IEEE, 2012, pp. 2911–2918. doi:[10.1109/CVPR.2012.6248018](https://doi.org/10.1109/CVPR.2012.6248018).

[87] S. Leutenegger, M. Chli, R. Y. Siegwart, BRISK: Binary robust invariant scalable keypoints, in: 2011 International conference on computer vision, IEEE, 2011, pp. 2548–2555. doi:[10.1109/ICCV.2011.6126542](https://doi.org/10.1109/ICCV.2011.6126542).

[88] P. F. Alcantarilla, A. Bartoli, A. J. Davison, KAZE Features, in: Computer Vision–ECCV 2012: 12th European Conference on Computer Vision, Florence, Italy, October 7–13, 2012, Proceedings, Part VI 12, Springer, 2012, pp. 214–227. doi:[10.1007/978-3-642-33783-3_16](https://doi.org/10.1007/978-3-642-33783-3_16).

[89] P. F. Alcantarilla, T. Solutions, Fast explicit diffusion for accelerated features in nonlinear scale spaces, in: British Machine Vision Conference, BMVC, BMVA Press, 2013, pp. 1281–1298. doi:[10.5244/C.27.13](https://doi.org/10.5244/C.27.13).

[90] E. Rublee, V. Rabaud, K. Konolige, G. Bradski, ORB: An efficient alternative to SIFT or SURF, in: 2011 International Conference on Computer Vision, IEEE, 2011, pp. 2564–2571. doi:[10.1109/ICCV.2011.6126544](https://doi.org/10.1109/ICCV.2011.6126544).

[91] J. Shi, et al., Good features to track, in: 1994 Proceedings of IEEE Conference on Computer Vision and Pattern Recognition, IEEE, 1994, pp. 593–600. doi:[10.1109/CVPR.1994.323794](https://doi.org/10.1109/CVPR.1994.323794).

[92] R. Ke, Z. Li, S. Kim, J. Ash, Z. Cui, Y. Wang, Real-time bidirectional traffic flow parameter estimation from aerial videos, *IEEE Transactions on Intelligent Transportation Systems* 18 (2016) 890–901. doi:[10.1109/TITS.2016.2595526](https://doi.org/10.1109/TITS.2016.2595526).

[93] D. DeTone, T. Malisiewicz, A. Rabinovich, SuperPoint: Self-Supervised Interest Point Detection and Description, in: 2018 IEEE/CVF Conference on Computer Vision and Pattern Recognition Workshops (CVPRW), 2018, pp. 224–236. doi:[10.1109/CVPRW.2018.00060](https://doi.org/10.1109/CVPRW.2018.00060).

[94] P.-E. Sarlin, D. DeTone, T. Malisiewicz, A. Rabinovich, SuperGlue: Learning Feature Matching With Graph Neural Networks, in: Proceedings of the IEEE/CVF conference on computer vision and pattern recognition, 2020, pp. 4938–4947. doi:[10.1109/CVPR42600.2020.00499](https://doi.org/10.1109/CVPR42600.2020.00499).

[95] M. A. Fischler, R. C. Bolles, Random sample consensus: A paradigm for model fitting with applications to image analysis and automated cartography, *Communications of the ACM* 24 (1981) 381–395. doi:[10.1016/B978-0-08-051581-6.50070-2](https://doi.org/10.1016/B978-0-08-051581-6.50070-2).

[96] M. Muja, D. G. Lowe, Fast approximate nearest neighbors with automatic algorithm configuration, in: International Conference on Computer Vision Theory and Applications, 2009, pp. 331–340. doi:[10.5220/0001787803310340](https://doi.org/10.5220/0001787803310340).

[97] R. Kumar, H. Sawhney, S. Samarasakera, S. Hsu, H. Tao, Y. Guo, K. Hanna, A. Pope, R. Wildes, D. Hirvonen, et al., Aerial video surveillance and exploitation, *Proceedings of the IEEE* 89 (2001) 1518–1539. doi:[10.1109/5.959344](https://doi.org/10.1109/5.959344).

[98] D. B. Barber, J. D. Redding, T. W. McLain, R. W. Beard, C. N. Taylor, Vision-based target geo-location using a fixed-wing miniature air vehicle, *Journal of Intelligent and Robotic Systems* 47 (2006) 361–382. doi:[10.1007/s10846-006-9088-7](https://doi.org/10.1007/s10846-006-9088-7).

[99] T. Toutin, Review article: Geometric processing of remote sensing images: models, algorithms and methods, *International journal of remote sensing* 25 (2004) 1893–1924. doi:[10.1080/0143116031000101611](https://doi.org/10.1080/0143116031000101611).

[100] D. Ekaso, F. Nex, N. Kerle, Accuracy assessment of real-time kinematics (RTK) measurements on unmanned aerial vehicles (UAV) for direct geo-referencing, *Geo-spatial information science* 23 (2020) 165–181. doi:[10.1080/10095020.2019.1710437](https://doi.org/10.1080/10095020.2019.1710437) CrossMark Logo CrossMark.

[101] R. Krajewski, J. Bock, L. Kloeker, L. Eckstein, The highD Dataset: A Drone Dataset of Naturalistic Vehicle Trajectories on German Highways for Validation of Highly Automated Driving Systems, in: 2018 21st International Conference on Intelligent Transportation Systems (ITSC), IEEE, 2018, pp. 2118–2125. doi:[10.1109/ITSC.2018.8569552](https://doi.org/10.1109/ITSC.2018.8569552).

[102] R. Makrigiorgis, P. Kolios, S. Timotheou, T. Theocharides, C. G. Panayiotou, Extracting the fundamental diagram from aerial footage, in: 2020 IEEE 91st Vehicular Technology Conference, IEEE, 2020, pp. 1–5. doi:[10.1109/VTC2020-Spring48590.2020.9128534](https://doi.org/10.1109/VTC2020-Spring48590.2020.9128534).

[103] O. Zheng, M. Abdel-Aty, L. Yue, A. Abdelraouf, Z. Wang, N. Mahmoud, CitySim: A Drone-Based Vehicle Trajectory Dataset for Safety-Oriented Research and Digital Twins, *Transportation Research Record* 2678 (2024) 606–621. doi:[10.1177/03611981231185768](https://doi.org/10.1177/03611981231185768).

[104] S. Kim, G. Anagnostopoulos, E. Barmpounakis, N. Geroliminis, Visual extensions and anomaly detection in the pNEUMA experiment with a swarm of drones, *Transportation Research Part C: Emerging Technologies* 147 (2023) 103966. doi:[10.1016/j.trc.2022.103966](https://doi.org/10.1016/j.trc.2022.103966).

[105] M.-R. Hsieh, Y.-L. Lin, W. H. Hsu, Drone-based object counting by spatially regularized regional proposal network, in: Proceedings of the IEEE International Conference on Computer Vision (ICCV), IEEE, 2017, pp. 4145–4153. doi:[10.1109/ICCV.2017.446](https://doi.org/10.1109/ICCV.2017.446).

[106] A. Kouris, C. Kyrkou, C.-S. Bouganis, Informed Region Selection for Efficient UAV-based Object Detectors: Altitude-aware Vehicle Detection with CyCAR Dataset, in: 2019 IEEE/RSJ International Conference on Intelligent Robots and Systems (IROS), IEEE, 2019, pp. 51–58. doi:[10.1109/IROS40897.2019.8967722](https://doi.org/10.1109/IROS40897.2019.8967722).

[107] R. Makrigiorgis, P. Kolios, C. Kyrkou, Aerial Multi-Vehicle Detection Dataset, 2022. doi:[10.5281/zenodo.7053442](https://doi.org/10.5281/zenodo.7053442).

[108] E. Puertas, G. De-Las-Heras, J. Fernández-Andrés, J. Sánchez-Soriano, Dataset: Roundabout aerial images for vehicle detection, Data 7 (2022) 47. doi:[10.3390/data7040047](https://doi.org/10.3390/data7040047).

[109] H. Yu, G. Li, W. Zhang, Q. Huang, D. Du, Q. Tian, N. Sebe, The unmanned aerial vehicle benchmark: Object detection, tracking and baseline, International Journal of Computer Vision 128 (2020) 1141–1159. doi:[10.1007/s11263-019-01266-1](https://doi.org/10.1007/s11263-019-01266-1).

[110] T. M. Tran, T. N. Vu, T. V. Nguyen, K. Nguyen, UIT-ADrone: A Novel Drone Dataset for Traffic Anomaly Detection, IEEE Journal of Selected Topics in Applied Earth Observations and Remote Sensing 16 (2023) 5590–5601. doi:[10.1109/JSTARS.2023.3285905](https://doi.org/10.1109/JSTARS.2023.3285905).

[111] P. Zhu, L. Wen, D. Du, X. Bian, H. Fan, Q. Hu, H. Ling, Detection and tracking meet drones challenge, IEEE Transactions on Pattern Analysis and Machine Intelligence 44 (2021) 7380–7399. doi:[10.1109/TPAMI.2021.3119563](https://doi.org/10.1109/TPAMI.2021.3119563).

[112] A. Bouguettaya, H. Zarzour, A. Kechida, A. M. Taberkit, Vehicle detection from uav imagery with deep learning: A review, IEEE Transactions on Neural Networks and Learning Systems 33 (2021) 6047–6067. doi:[10.1109/TNNLS.2021.3080276](https://doi.org/10.1109/TNNLS.2021.3080276).

[113] T.-Y. Lin, M. Maire, S. Belongie, J. Hays, P. Perona, D. Ramanan, P. Dollár, C. L. Zitnick, Microsoft COCO: Common Objects in Context, in: Computer Vision–ECCV 2014: 13th European Conference, Zurich, Switzerland, September 6–12, 2014, Proceedings, Part V 13, Springer, 2014, pp. 740–755. doi:[10.1007/978-3-319-10602-1_48](https://doi.org/10.1007/978-3-319-10602-1_48).

[114] W. Hao, S. Zhili, Improved mosaic: Algorithms for more complex images, Journal of Physics: Conference Series 1684 (2020) 012094. doi:[10.1088/1742-6596/1684/1/012094](https://doi.org/10.1088/1742-6596/1684/1/012094).

[115] Y. Jin, D. Mishkin, A. Mishchuk, J. Matas, P. Fua, K. M. Yi, E. Trulls, Image matching across wide baselines: From paper to practice, International Journal of Computer Vision 129 (2021) 517–547. doi:[10.1007/s11263-020-01385-0](https://doi.org/10.1007/s11263-020-01385-0).

[116] U. Efe, K. G. Ince, A. A. Alatan, Effect of parameter optimization on classical and learning-based image matching methods, in: Proceedings of the IEEE/CVF International Conference on Computer Vision, IEEE Computer Society, Los Alamitos, CA, USA, 2021, pp. 2506–2513. doi:[10.1109/ICCVW54120.2021.00283](https://doi.org/10.1109/ICCVW54120.2021.00283).

[117] S. P. Venturuthiyil, M. Chunchu, Vehicle path reconstruction using Recursively Ensembled Low-pass filter (RELP) and adaptive tri-cubic kernel smoother, Transportation Research Part C: Emerging Technologies 120 (2020) 102847. doi:[10.1016/j.trc.2020.102847](https://doi.org/10.1016/j.trc.2020.102847).

[118] H. E. Rauch, F. Tung, C. T. Striebel, Maximum likelihood estimates of linear dynamic systems, AIAA Journal 3 (1965) 1445–1450. doi:[10.2514/3.3166](https://doi.org/10.2514/3.3166).

[119] J. Zhang, H. Yang, Z. Chen, T. Yu, H. Liu, Probability distribution and recommended values of passenger car external dimensions in mechanical parking garage design, Journal of Asian Architecture and Building Engineering 21 (2022) 1942–1958. doi:[10.1080/13467581.2021.1971995](https://doi.org/10.1080/13467581.2021.1971995).

[120] H. Su, S. Liu, B. Zheng, X. Zhou, K. Zheng, A survey of trajectory distance measures and performance evaluation, The VLDB Journal 29 (2020) 3–32. doi:[10.1007/s00778-019-00574-9](https://doi.org/10.1007/s00778-019-00574-9).

[121] P. D. Groves, Shadow matching: A new GNSS positioning technique for urban canyons, The journal of Navigation 64 (2011) 417–430. doi:[10.1017/S0373463311000087](https://doi.org/10.1017/S0373463311000087).

[122] E. Kaplan, C. Hegarty, Understanding GPS/GNSS: Principles and Applications, 3rd ed., Artech House, USA, 2017.

[123] A. Savitzky, M. J. Golay, Smoothing and differentiation of data by simplified least squares procedures, *Analytical chemistry* 36 (1964) 1627–1639. doi:[10.1021/ac60214a047](https://doi.org/10.1021/ac60214a047).